Theoretical model for nonlinear photonic topological insulators

Ghada H. Alharbi

A thesis presented for the degree of

Doctor of Philosophy

School of Physics and Astronomy

Cardiff University

December 2024

Under the supervision of:

- Dr. Sang Soon Oh

For my niblings

Abstract

Over the past few years, nonlinear topological photonics have garnered significant attention due to their intriguing properties and potential applications. Research in nonlinear topological photonics has revealed a variety of interesting phenomena, including nonlinearity-induced topological phase transitions, the formation of edge solitons, and the influence of the Kerr effect on the emergence of edge modes. This thesis focuses on investigating the spontaneous symmetry breaking of counter-propagating light, specifically between clockwise (CW) and counterclockwise (CCW) modes, within the framework of a one-dimensional Su-Schrieffer-Heeger (SSH) model consisting of optical ring resonators with Kerr nonlinearity. The approach in this thesis is based on the Lugiato-Lefever equation, which we extended to describe the field amplitudes in each ring resonator for both CW and CCW modes, considering small and large cross-phase modulation (XPM) strength. With a small XPM strength, one can demonstrate the optical bistability of the edge mode. However, with large XPM strength, when the coupling between CW and CCW modes becomes stronger, we observed complex dynamics in light propagation as well as optical bistability. Strong nonlinearity via XPM with the associated high pump intensity leads to excitation of the bulk modes for large detuning values, showing periodic and chaotic oscillations. As there are many parameters that can affect the spontaneous symmetry breaking of counter-propagating light through nonlinear SSH lattice, we will present phase

diagrams depending on variant parameters: input intensity, XPM strength, coupling with sources, and intercell coupling coefficient. Then, we will compare the dynamic of the nonlinear SSH lattice with identical coupling coefficients. Further, to investigate the system in depth, we will apply a data-driven method called dynamical mode decomposition, which extracts spatial modes. The study of nonlinear topological photonics and spontaneous symmetry breaking in optical SSH lattices paves the way for applications such as robust optical isolators and circulators, all-optical memory and switching devices.

Acknowledgements

During my PhD, I have learned enormously from my supervisor Dr. Sang Soon Oh. I am deeply indebted to him for his academic guidance, patient teaching, and support. He has provided me with guidance, assistance, valuable feedback, encouragement, and expertise that I have needed during my PhD journey.

I am thankful to Prof. Zain Yamani for his support and advice. I am also grateful to my second supervisor, Dr. Egor Muljarov, and my mentor, Dr. Freeke van de Voort, for their time and advice.

I would like to extend my thanks to my colleague Dr. Stephan Wong for the insightful discussions and valuable feedback. I am also thankful to my colleagues Dr. Yongkang Gong, Dr. Haedong Park, Dr. Ananya Ghatak, Dr. Zeeshan Ahmad, Dr. Shaikhah Almousa, Kyle Netherwood, Amal Aldhubaib and Ion Wood-Thanan for support and the interesting discussions.

I am extremely grateful to my family for their constant love and endless support, and to my grandmothers for their prayers and words of wisdom.

Finally, I am thankful to the University of Tabuk for their support with the scholarship.

Puplication & presentaions

Puplication

- Ghada H. Alharbi, Stephan Wong, Yongkang Gong and Sang Soon Oh. Asymmetrical temporal dynamics of edge modes in Su-Schrieffer-Heeger lattice with Kerr nonlinearity. Physical Review Research 6, L042013 (2024).

Presentations at Peer-reviewed International Conferences

- Ghada Alharbi and Sang Soon Oh. "Asymmetrical temporal dynamics of topological edge modes in Su-Schrieffer-Heeger lattice with Kerr nonlinearity". Photon 2024, Swansea, Wales (2024), poster.

- Ghada Alharbi, Sang Soon Oh. "Optical bistability in Su-Schrieffer-Heeger lattice with Kerr nonlinearity". META, Paris, France (2023), poster.

- Ghada Alharbi, Stephan Wong, Yongkang Gong and Sang Soon Oh. "Bistability in Photonic Topological Insulators with Kerr Nonlinearity". CLEO: Applications and Technology, California, United States (2021), poster.

- Ghada Alharbi and Sang Soon Oh. "Modelling bistability in 1D array of coupled micro-ring resonators". SIOE: Semiconductor and Integrated Optoelectronics, Cardiff, UK (2021), poster.

- Ghada Alharbi and Sang Soon Oh. "Bistability in photonic topological insulator with Kerr nonlinearity". Photon (2020), Birmingham, UK (2020), oral.

List of Figures

Contents

Chapter 1

Introduction

Topological physics introduces novel phases of matter characterized by topological invariants that persist under continuous changes, such as twisting or bending. These phases include phases of topological insulators, topological superconductors, and semimetals, each featuring distinctive surface or edge states not found in conventional materials. The edge (or surface) states have an extraordinary immunity against defects and disorders arising from topological invariants such as the Chern number. The field of topological physics in condensed matter has rapidly advanced since Klaus von Klitzing discovered the quantum Hall effect in 1980 [1]. In the quantum Hall effect, a two-dimensional electron gas is placed in a strong perpendicular magnetic field at low temperatures, resulting in quantized Hall conductivity as the conductivity is proportional to the magnetic field intensity. The strong magnetic field breaks time-reversal symmetry. Consequently, current is carried by electrons confined along the edges of the system, which are called edge states. The states exhibit unidirectional propagation and are immune to disorder and defects.

In the topological photonics field, which started in 2009 [2], analogous principles are applied to light. Similar to topological edge states in condensed matter physics, photonic topological modes are localized at the boundaries of two different photonic topological insulators. In such a photonic system, the edge modes confine light to propagate unidirectionlly with broken of the time-reversal ($\mathcal{TR}$) symmetry without scattering or in counter-propagating directions with $\mathcal{TR}$ symmetry preserved. Similar to topological insulators, edge modes are protected by a nonzero Chern number in systems with broken $\mathcal{TR}$ symmetry while $\mathbb{Z}_2$-invariance persists in systems with $\mathcal{TR}$ symmetry preserved. This protection grants immunity from certain defects and disorder. The main motivation for implementing topological phases in a photonic system is remarkable immunity. This immunity enables robust light transmission, even with fabrication imperfections or environmental fluctuations or fabrication surface roughness [3]. Additionally, the design of these systems can lead to novel applications, such as low-loss waveguides and robust photonic circuits [4].

It is important to emphasize that photonics can enrich topological phases with unique properties, including nonlinearities and non-Hermiticity, resulting from the intense interaction between light and matter. Because topological features remain unchanged under continuous transformations, topological photonic systems are anticipated to exhibit a level of resilience to disorder and imperfections that do not typically exist in conventional photonic devices. Implementing topological insulators in optical platforms allows researchers to study and utilise the robustness of these edge modes in applications of localized and topological modes such as optical cavities and waveguide arrays.

In recent years, many review papers have been published on photonic topological insulators [4–8], covering basic concepts, structures and optical platforms. There are several ways to construct photonic versions of topological insulators [5–10], using optical platforms such as waveguide [11–22], cavities [23–28], ring resonators arrays [29] and plasmonic and dielectric nanoparticles [30–32]. These methods can be divided into two types: $\mathcal{TR}$ symmetry-broken systems, which need an external magnetic bias or time modulation, and time-reversal symmetry preserved routes without the presence of the magnetic field [3, 33–36]. In 2008, F. D. M. Haldane and S. Raghu presented the first theoretical prediction of edge mode in optics in photonic crystals analogous to the Hall structure [37, 38]. They proposed that by using nonreciprocal (Faraday effect) media, which breaks time-reversal symmetry, it is possible to create photonic band gaps (PBGs) in two-dimensional photonic crystals. These PBGs are characterized by a topological invariant known as the Chern number, which determines the presence of unidirectional photonic modes at the interface between two different PBG media. The proposal was then confirmed experimentally in 2009, and edge modes were observed at the interface between different types of photonic crystals in a 2D array, consisting of a magneto-optical and regular photonic crystal in a microwave regime [2]. Here the optical edge modes are shown by transmission spectra in clockwise and counter-clockwise directions. Since the magnetic field has weak effects on $\mathcal{TR}$ symmetry broken at optical frequencies, many studies have focused on photonic topological insulators free of an external magnetic field. Constructing a photonic topological insulator with $\mathcal{TR}$ symmetry can be applied widely in different optical platforms such as waveguides, couple ring resonators and metamaterials. For example, Rechtsman *et al.* experimentally demonstrated photonic Floquet topological insulators: a honeycomb lattice consisting of evanescently coupled helical waveguides [33].

Over the past few years, the framework of research on photonic topological insulators has been extended to nonlinear regimes [11, 39–46]. The simplest model that presents a nonlinear photonic topological insulator is a 1D Su-Schrieffer-

Heeger (SSH) model with the Kerr effect. It can be implemented in a lattice of optical elements, considering Kerr nonlinearity in on-site potentials or with the coupling coefficients [12, 14, 21, 22, 28, 41, 47–55]. Dobrykh *et al.* experimentally showed how nonlinearity could tune the linear topological edge states in an SSH lattice of coupled resonators with Kerr nonlinearity on-site [41]. Increasing input power led to a frequency shift (blue shift) for the edge state. Also, the induced topological transition has been observed in a coupled waveguide array based on SSH with a domain wall [14]. Due to the intrinsic configurability of nonlinear structures where Kerr nonlinearity is considered in the coupling coefficients, changes in excitation intensity can lead to topological phase transitions. These transitions result in the emergence of topologically robust edge states [47, 49]. Ma and Susanto demonstrated the observation of edge solitons and showed that, depending on the ratio coupling, edge solitons can be stable or unstable (oscillate) [52]. Topological solitons can emerge from the linear topological mode of the SSH lattice, whether in the presence of self-focusing or self-defocusing nonlinearity, as long as the nonlinearity remains weak [50]. A theoretical model has been presented to describe, based on coupled mode theory, weak and strong Kerr effect on-site on a lattice of waveguide [12]. Periodic oscillations between two edge modes take place when nonlinearity is moderate. Once Kerr nonlinearity is increased, the system exhibits chaotic oscillations as a result of strong interaction between edge and bulk modes.

So far, the mechanisms through which clockwise (CW) and counterclockwise (CCW) symmetries are broken in many coupled ring resonators have not been thoroughly investigated. Most research has concentrated on configurations involving only one or two ring resonators with Kerr nonlinearity [56–61].

Kerr nonlinearity can lead to asymmetrical behaviors in optical ring resonators. Asymmetrical optical bistability in a nonlinear Sagnac interferometer was theoretically predicted by Kaplan and Meystre [57]. The Sagnac interferometer is symmetrically pumped by two beams of equal intensity but in opposite directions, showing different regimes of bistability and multistability due to the non-reciprocal propagation of counterpropagating waves. In 2017, Del Bino *et al.* [62] presented the experimental realization of optical bistability in a nonlinear ring resonator based on the Kerr effect. Here, bi-directional laser pumping into a ring resonator from one side in opposite directions leads to spontaneous symmetry breaking between clockwise and counterclockwise light that propagates through the resonator [62]. Moreover, the Kerr ring resonator displays oscillations, including chaotic and periodic [58, 60]. Scanning a variety of detuning with high input intensity into an optical ring resonator shows different regimes of oscillations with or without self-switching.

In this thesis, we aim to investigate spontaneous symmetry breaking in counter-propagating light through a 1D photonic topological insulator lattice. We first present an analytical system for a one-dimensional photonic topological insulator with on-site Kerr nonlinearity, implementing a Su-Schrieffer-Heeger model in an optical ring resonator array. To investigate the spontaneous symmetry breaking in optical intensity for edge modes, we consider self-phase modulation and cross-phase modulation effects. We explain the optical bistability and analyze the temporal dynamic of our structure. We plot phase diagrams for a nonlinear photonic topological insulator system using Poincaré sections.

This thesis is organised as follows:

In **Chapter two**, we provide the reader with background concepts related to a Su-Schrieffer-Heeger model and Kerr effect. First, we present the Hamiltonian of a linear model, showing an energy diagram for the nontrivial topological phase. Also, we explain the zero-energy state as the signature characterization of topological phase. Second, we explain the Kerr effect, including self modulation and cross modulation. To investigate how Kerr nonlinearity affect the field amplitude in ring resonators, we explain the Lugiato-Lefever model.

Chapter three is related to our paper Reference no.[63]. we present the first chapter of our scientific result for the Su-Schrieffer-Heeger model with Kerr effect. To investigate the effect of Kerr nonlinearity, we have numerically solved the Lugiato-Lefever equations. We have investigated two situations depending on the input sources. In the first case, two identical sources are placed on the left side of the SSH lattice. In the second case, we used four identical sources, two sources on each side.

Chapter four We show complex behaviors of intensity, including periodic and chaotic oscillations. We have plotted Poincaré sections for maxima intensities as a function of detuning at a large value of cross-phase modulation strength. We have shown how input power can affect the propagation of light. Moreover, we have investigated the transition of the system from stable to unstable when the system displays chaotic oscillations.

Chapter five We have applied more analysis to present phase diagrams for various of parameters. We have compared nonlinear SSH lattice with symmetric and asymmetric coupling coefficients. In addition, we used dynamical mode decomposition to analyze time sets data, which we collected from the results of the previous chapter, chapter four.

In the last chapter, **chapter 6**, we have highlighted our significant results and future research directions.

Chapter 2

Theoretical Background

2.1 One-dimensional photonic topological insulator model

In condensed matter physics, the Su-Schrieffer-Heeger (SSH) model, which was proposed in 1979 by Su, Schrieffer, and Heeger, has become a foundational concept in the study of topological phases of matter. It was initially introduced in chemistry to study solitons in polyacetylene, a chain of carbon atoms with alternating strong and weak bonds, as illustrated in Fig. 2.1(a) [64]. The SSH model is one of the simplest models that present a topological insulator phase. It offers deep insights into topological phases of matter through understanding bulk-boundary correspondence, topological invariants, and edge states [65].

In photonics, one can implement a topological insulator model using optical elements, such as coupled optical ring resonators [29], waveguides [11–22, 66] and electromagnetic metamaterials [67, 68]. Therefore, the SSH model describes a one-dimensional chain of optical elements where light propagates and couples between adjacent sites, similar to how electrons move through an atomic lattice

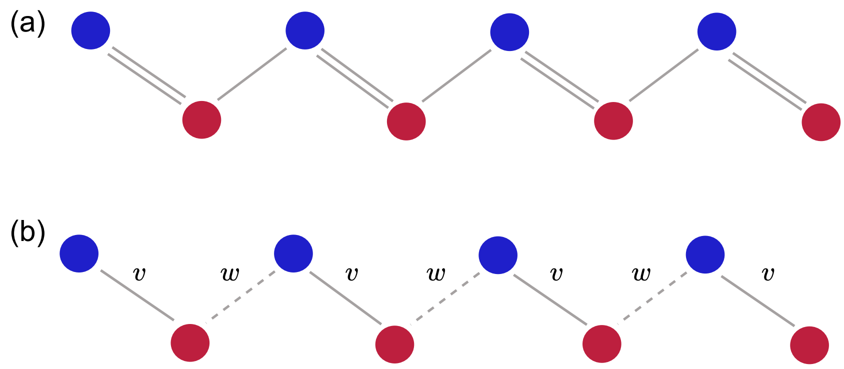

Figure 2.1: SSH model, blue and red circles refer to A and B sublattices, respectively. (a) for polyacetylene. (b) the SSH model consists of an optical element in each site with coupling strength v and w.

by hopping from one site to another. The coupling strength between optical elements are inter- and intra-cell coupling strengths, v and w respectively, as shown in Fig. 2.1(b). Each unit cell contains two optical elements: one in sublattice A and another in sublattice B. The introduction of alternating coupling strengths is also called dimerization because the two atoms that belong to different sublattices, A and B, form one unit cell.

2.1.1 SSH Hamiltonian

The Hamiltonian of finite 1D SSH lattice with open boundary conditions in real space is given by:

$$\hat{\mathbf{H}} = \sum_{n=1}^{N} \left[\mu \hat{a}_n^\dagger \hat{a}_n + \mu \hat{b}_n^\dagger \hat{b}_n + (v \hat{a}_n^\dagger \hat{b}_n + w \hat{a}_{n+1} \hat{b}_n^\dagger + h.c.)\right], \tag{2.1}$$

where the first two terms stand for on-site energy with μ. $\hat{a}_n$ ($\hat{a}_n^\dagger$) and $\hat{b}_n$ ($\hat{b}_n^\dagger$) are creation (annihilation) operators in the different sublattices A and B within the unit cell n, respectively; v and w stand for the intracell and intercell hopping, respectively. The Hamiltonian Eq. 2.1 for N unit cell can be written in a matrix

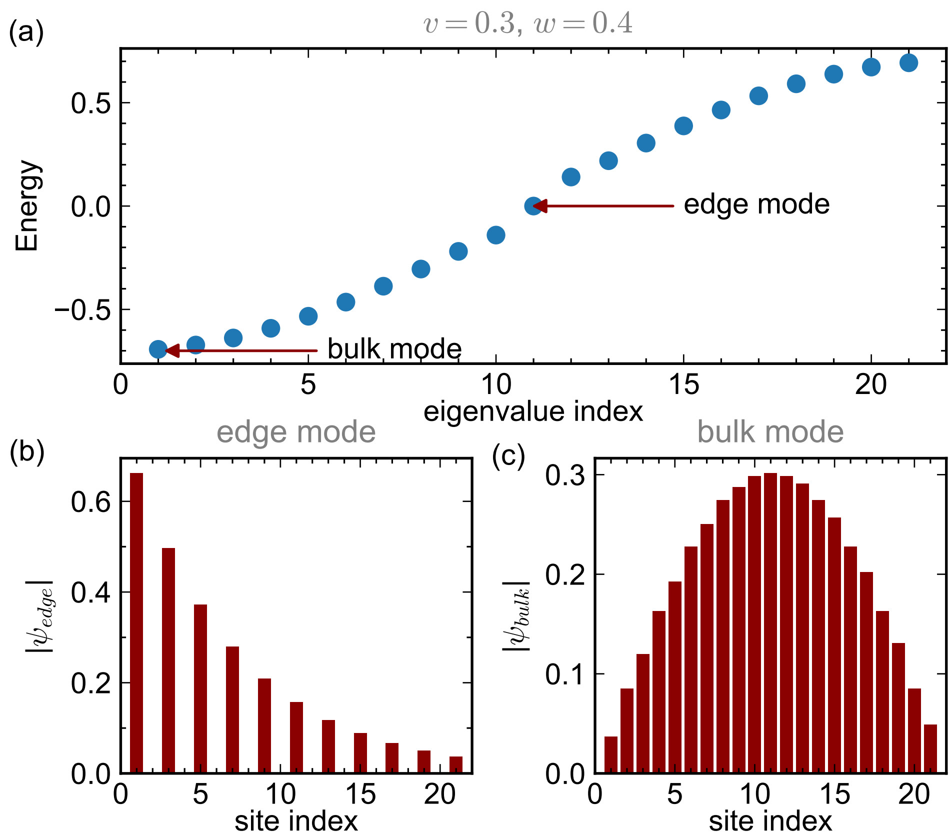

Figure 2.2: (a) Energy spectrum for topologically nontrivial case ($v = 0.3$, $w = 0.4$) for $M = 2N + 1 = 21$. Profile of the zero-energy edge mode in (b), of the bulk mode in (c).

form as:

$$\hat{\mathbf{H}} = \begin{pmatrix} \mu & v & 0 & 0 & \dots & 0 \\ v & \mu & w & 0 & \dots & 0 \\ 0 & w & \mu & v & \dots & 0 \\ 0 & 0 & v & \mu & \ddots & \vdots \\ \vdots & \vdots & \vdots & \ddots & \ddots & v \\ 0 & 0 & 0 & \dots & v & \mu \end{pmatrix}. \tag{2.2}$$

The eigenvalues (energies) of the Hamiltonian for a chain containing 21 optical elements with zero on-site energy are shown in Fig. 2.2(a). One can obtain the momentum space Hamiltonian of the SSH chain, considering the infinite size of the chain and applying Bloch's periodic boundary condition. It requires considering one unit cell (2 sublattices A and B). Then, we can write the bulk Hamiltonian as :

$$\mathbf{H}(k) = \begin{pmatrix} \mu & \mathbf{h}^*(k) \\ \mathbf{h}(k) & \mu \end{pmatrix}, \tag{2.3}$$

where $\mathbf{h}(k) = v + we^{ika}$, k is the wavenumber and a is the lattice constant. For real values of v and w and considering zero onsite energy i.e. $\mu = 0$, the eigenvalues are given by:

$$E(k) = \pm\sqrt{|\mathbf{h}(k)|^2}, \tag{2.4}$$

$$E(k) = \pm\sqrt{v^2 + w^2 + 2vw\cos(ka)}. \tag{2.5}$$

It is clear that the energy band diagram depends on v and w values. The plots in Fig. 2.3(a,b,c) show that the SSH lattice has an energy band gap when $v > w$ or $v < w$. When the Fermi level lies in the band gap, the SSH lattice becomes an insulator. However, when $v = w$, it becomes a conductor because there is no bandgap. The system is a conductor with symmetry hopping, when $v = w$.

The momentum space Hamiltonian is a two-dimensional Hermitian matrix that can be written in terms of Pauli matrices $\sigma = (\sigma_x, \sigma_y, \sigma_z)$ as:

$$\mathbf{H}(k) = \mathbf{h}(k)\sigma. \tag{2.6}$$

The components of $H(k)$ can be defined as:

$$h_x(k) = v + w\cos(ka), \qquad h_y(k) = w\sin(ka), \qquad h_z(k) = 0,$$

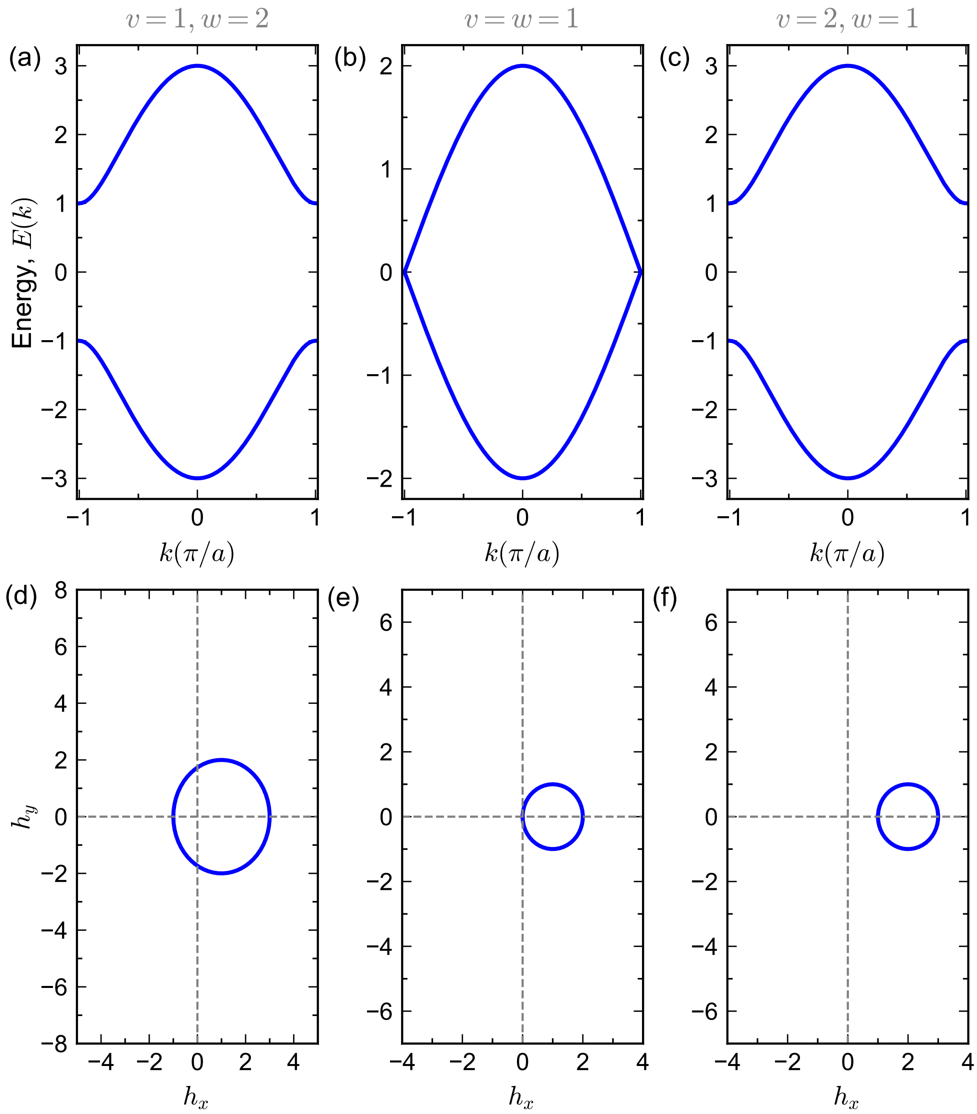

Figure 2.3: Energy band diagrams for different coupling constants. (a,d) correspond to the nontrivial SSH lattice, encircling the origin of coordinates in (d) yields a winding number (topological invariant) value of 1. (b,e) correspond to the gapless band energy for $v = w$. (c, f) correspond to the trivial phase with zero winding number as the origin of coordinates is not encircled in (f).

with the direction of $\mathbf{h}(k)$ given by:

$$\phi = \tan^{-1}\frac{h_y}{h_x} = \tan^{-1}\left(\frac{w\sin(ka)}{v + w\cos(ka)}\right).$$

Figure 2.3(d,e,f) illustrates three different paths of $h(k)$ over the first Brillouin zone. Since the Brillouin zone is 1D periodic with respect to k, $\mathbf{h}(k)$ forms a closed loop. Obviously, for $v < w$ and $v > w$, there are two distinct paths, despite both paths having similar band energy diagrams. The path encircles the origin for the nontrivial topological phase, i.e. $v < w$, whereas in the trivial phase, i.e. $v > w$, it does not encircle the origin. From this trajectory, we can determine graphically the winding number, which counts the number of times the loop surrounds the origin of the h_x, h_y plane. Here, the origin point is localized at $\mathbf{h}(k) = 0$. Mathematically, the calculation of the total phase change of the complex function $h(k)$ over the Brillouin zone is known as the winding number (W). It is a topological invariant that can be defined as:

$$W = \frac{1}{2\pi}\int_{-\pi}^{\pi}\frac{d}{dk}\arg[\mathbf{h}(k)]\,dk.$$

The Winding number can take on values of either 0 or 1, depending on intercell and intracell parameters. It will be zero for the trivial phase ($v > w$) and 1 for the nontrivial topological phase ($w > v$).

2.1.2 Chiral symmetry (sublattice symmetry)

In the SSH model, chiral symmetry is also referred to as sublattice symmetry [65]. The SSH chain contains two sublattices, A and B, in each unit cell; it is not allowed to couple from A to A and B to B. The Hamiltonian of this system

(2.1) ($\mu = 0$) has a chiral symmetry if it satisfies the following condition:

$$\hat{\Gamma}\hat{\mathbf{H}}\hat{\Gamma}^{\dagger} = -\hat{\mathbf{H}}, \tag{2.7}$$

where $\hat{\Gamma}$ is unitary $\hat{\Gamma}^2 = 1$, and satisfies anti-commuting $\{\hat{\Gamma}, \hat{\mathbf{H}}\} = 0$. As a result of the chiral symmetry, for each energy state ϵ, there is a state with energy $-\epsilon$ as long as we have an energy gap. Figure 2.2 (a) shows the chiral symmetry in the energy spectrum from solving the eigenvalues problem of Eq. 2.1 for 21 sites. The energy states are divided into two bands, with a bandgap in the middle hosting one zero-energy state. Here, there is one zero-energy state because we have an odd number of sites; for an even number of sites, there are two zero-energy states. This zero energy is the signature of the nontrivial topological phase, known as topological zero-energy mode.

2.1.3 Edge mode

An edge mode is an essential characteristic of a topologically nontrivial SSH lattice. It is protected against perturbations even with defects or disorders by the bulk-boundary correspondence, which links the existence of zero-energy states at the edges to the topological invariant of the bulk, i.e. the winding number [65]. For a finite SSH lattice, described by Eq. 2.8, the chiral (sublattice) symmetry is preserved, as indicated by the relation $\hat{\Gamma}\hat{\mathbf{H}}\hat{\Gamma}^{\dagger} = -\hat{\mathbf{H}}$, where $\Gamma = \mathrm{diag}[1, -1, 1, -1, \ldots]$. This symmetry implies that for every eigenstate $|\Psi_n\rangle$ with energy E_n, there exists a corresponding eigenstate $\Gamma|\Psi_n\rangle$ with energy $-E_n$. This ensures the existence of zero-energy eigenstates (unpaired) for an SSH lattice with odd site numbers. Furthermore, these zero-energy states are also eigenstates of the chiral symmetry operator Γ. As a result, the zero-energy eigenstates can exist entirely on one sublattice, making the amplitudes at odd (even) sites non-

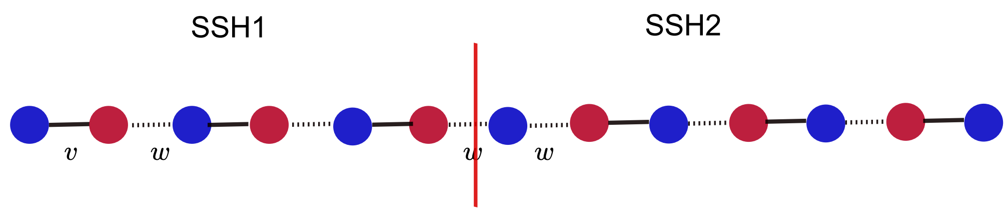

Figure 2.4: Schematic of the SSH model with wall domain.

zero (zero) [65]. Figure 2.2(b) and 2.2(c) show that the distribution of the zero edge mode decreases gradually with zero amplitude at an even site (sublattice B) while bulk mode propagates through the bulk of the SSH lattice. The zero edge state is protected by chiral symmetry and winding number equal to 1; the edge states will pin at zero energy as long as the chiral symmetry is preserved [69].

However, the zero-edge mode is localized not only at the end of the SSH system but also at the interface between two domains [65], as shown in Fig. 2.4 where the winding numbers differ. This example of the SSH lattice has $v > w$ on the left-hand side with winding number $W = 0$ (trivial phase) while on the right side with the winding number is $W = 1$ (non-trivial phase), and the domain wall is located where the coupling parameters are swapping. The Hamiltonian of such a system is given by:

$$\hat{\mathbf{H}} = \sum_{n=1}^{N}(\mu\hat{a}_n^{\dagger}\hat{a}_n+\mu\hat{b}_n^{\dagger}\hat{b}_n)+\sum_{n\geq m}^{N}(v\hat{a}_n^{\dagger}\hat{b}_n+w\hat{a}_{n+1}\hat{b}_n^{\dagger}+h.c.)+\sum_{n\leq m}^{N}(w\hat{a}_n^{\dagger}\hat{b}_n+v\hat{a}_{n+1}\hat{b}_n^{\dagger}+h.c.), \tag{2.8}$$

where m indicates where the domain wall is located. Figure 2.5(a) shows that the energy diagram of the SSH with a domain wall has one zero-energy mode. The field distribution of edge mode is concentrated at the interface between the SSH lattices as shown in Fig. 2.5(b).

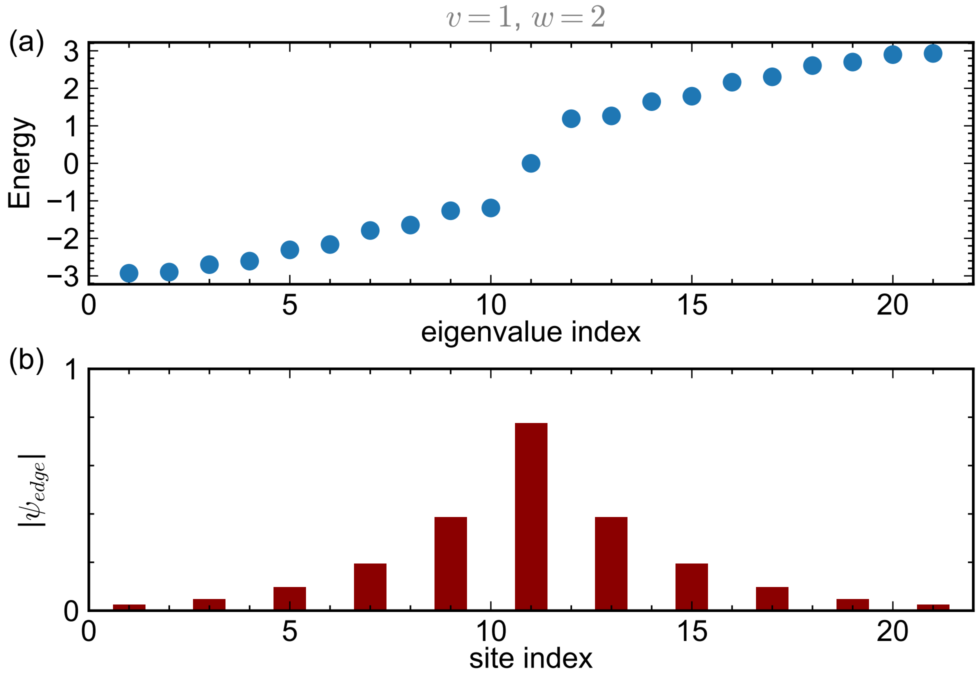

Figure 2.5: (a) Energy spectrum for SSH with wall domain. (b) The field distribution of the edge mode.

2.2 Kerr effect

The Kerr effect, named after John Kerr, a Scottish physicist, refers to the change of refraction that depends on the intensity of light. In 1875, he observed the change in the polarisation of light when an electric field is applied to an isotropic and transparent material [70]. Depending on the source of the applied electric field, the Kerr effect can be divided into two types: the electro-optic Kerr effect and the optical Kerr effect. In the case of the electro-optic Kerr effect, a varying electric field from the voltage source is applied to material, e.g., water, causing a change in the refractive index. In the optical Kerr effect, a strong linearly polarised electric field induces nonlinear polarisation in the medium, resulting in optical birefringence, i.e., different refractive indices in two perpendicular directions to light polarisation [71]. This change in refractive index (Δn)

can be written in terms of the optical intensity (I) in the nonlinear medium as $\Delta n = n_0 + n_2 I$, where n_0 is the linear refractive index (or the weak intensity index) and n_2 is the nonlinear refractive index (also known as Kerr index) [72]. As the nonlinear term is much smaller than the linear term, the essential requirement of the optical Kerr effect is a high optical power source such as lasers.

After the invention of the laser by Theodore Maiman [73], the optical Kerr effect has been experimentally observed using two linearly polarised laser beams: one intense beam for inducing the birefringence and the other weak one as a probe of the birefringence [74, 75]. The intense beam induces an extraordinary axis in the isotropic material through the nonlinear refractive index, while the weak probe beam does not change the refractive index [76]. This intense beam can modify the refractive indices that a probe beam and its own wave experience, known as self-phase (SPM) modulation and cross-phase modulation (XPM), respectively.

Self-phase modulation arises from the change in the refractive index of the light beam by itself. Mathematically, it can be written as :

$$\Delta n = n_2 I \tag{2.9}$$

where n_2 is a nonlinear index.

Cross-phase modulation arises from the interaction between at least two beams of light with high intensities. Then the optical phase of a light beam is altered due to its interaction with another beam in a nonlinear medium. This refers to a change in the refractive index:

$$\Delta n = 2n_2 I. \tag{2.10}$$

By comparing with SPM, there is a factor of 2 because the phase shift in cross-phase modulation is twice as strong as in self-phase modulation for the same intensity. To explain the origin of factor 2 in XPM [56], from the third nonlinear polarization P^{NL} which is written as:

$$P^{NL} = \chi^{(3)} E|E|^2, \tag{2.11}$$

where $\chi^{(3)}$ is the nonlinear susceptibility, and E is the total electric field of counter-propagating light which is given by:

$$E = E_{cw} e^{ikx} + E_{ccw} e^{-ikx}. \tag{2.12}$$

By substituting this definition into Eq. 2.11:

$$P^{NL} = \chi^{(3)}(E_{cw} e^{ikx} + E_{ccw} e^{-ikx})[(E_{cw}^2 + E_{ccw}^2) + (E_{cw} E_{ccw} e^{2ikx} + c.c)] \tag{2.13}$$

$$P^{NL} = \chi^{(3)} E_{cw} e^{ikx}(|E_{cw}|^2 + 2|E_{ccw}|^2) + \chi^{(3)} E_{ccw} e^{-ikx}(|E_{ccw}|^2 + 2|E_{cw}|^2]) \tag{2.14}$$

We consider both SPM and XPM in this work, setting the XPM constant to 2 and larger than 2 in the chapter 3 and chapter 4.

2.3 Optical ring resonator

In 1969, E.J.M. Marcatili first proposed an optical ring resonator which consists of a straight waveguide and ring resonator [77]. An optical ring resonator guides light using total internal reflection and allows it to circulate independently in

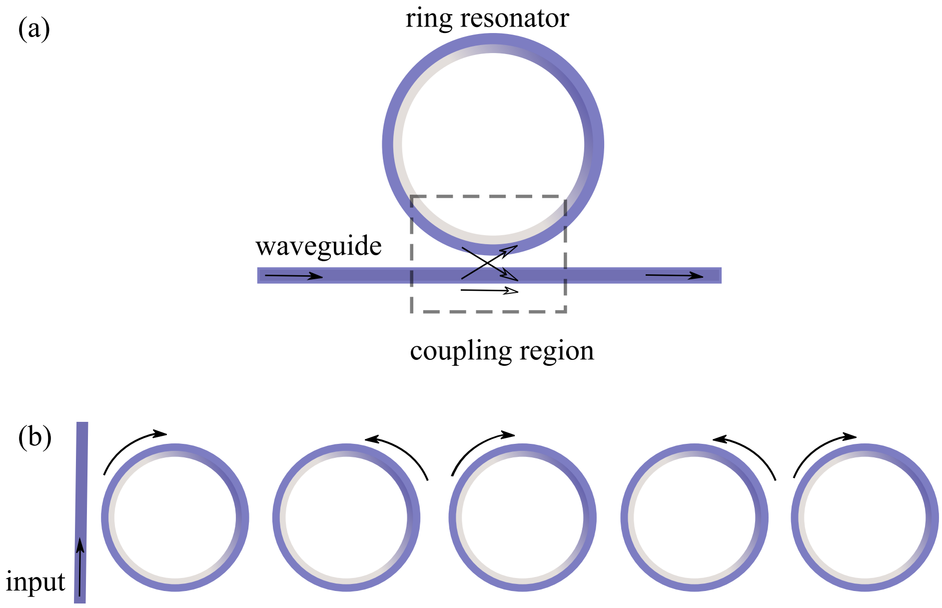

Figure 2.6: (a) All-pass and (b) Coupled-Resonator Optical Waveguide (CROW) based on optical ring resonators.

two opposite directions. A basic optical ring resonator setup consists of a single straight waveguide coupled with a circular resonator, as shown in Fig. C.1(a). This configuration functions as an all-pass filter [78]. When light travels through the waveguide, a portion of it couples into the ring resonator at the coupling region via the evanescent field. After circulating within the ring, part of the light coupled back into the waveguide, where it interferes with the incoming optical wave.

When multiple ring resonators are coupled in an array, they form the coupled-resonator optical waveguides which called CROW system [79, 80], as shown in Fig. C.1(b). In a CROW, the light wave propagates by jumping between adjacent resonators through weak coupling, analogous to electron hopping in tight-binding models in solid-state physics. In this work, we use this CROW to implement an optical SSH lattice.

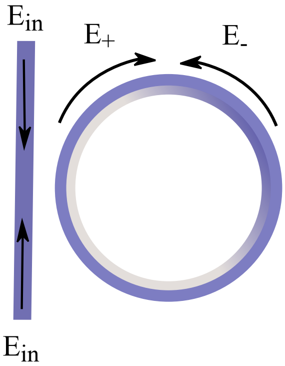

Figure 2.7: Schematic of the Kerr ring resonator.

2.4 Symmetry breaking in micro-ring resonator

Pumping a micro-ring resonator, which is made of a nonlinear medium, by two identical laser beams as illustrated in Fig. 2.7 induces a change in the refractive index, results in a resonance frequency shift. The Kerr effect causes a change in the resonance frequency of the two counter-propagating modes as a result of SPM and XPM, and the coupling via XPM between them leads to spontaneous symmetry breaking above a certain threshold of the input intensity. Asymmetrical behaviors include bistability, multistability, and periodic and chaotic oscillations. To observe such asymmetrical behaviors in the Kerr ring resonator, there are two common ways: first, using counter-propagating light intensities, and second, using two orthogonal polarized light components [62, 81]. The first way depends on injecting symmetrical light beams into the ring resonator from two different directions. In the second mechanism, the ring resonator is pumped by linearly polarised input fields [82]. Here, in this work, we will consider the first method. The dynamic equation that describes the field amplitude in a passive ring resonator with Kerr nonlinearity is given by the Lugiato-Lefever model[83]:

$$\frac{\partial E_{\pm}}{\partial \bar{t}} = E_{in} - E_{\pm} - i\Delta E_{\pm} + i\eta E_{\pm}\Big(|E_{\pm}|^2 + 2|E_{\mp}|^2\Big) + i\beta\frac{\partial^2 E_{\pm}}{\partial \bar{\tau}^2}, \tag{2.15}$$

where $\pm$ signs indicate, respectively clockwise and counterclockwise directions, $\bar{t} = \gamma t$, γ is the cavity decay, E_{in} is the input field, Δ the detuning, $\eta = +1$ for self-focusing medium and $\eta = -1$ for self-defocusing medium, and τ is the fast time during a round trip. On the right-hand side, the second term is decay, the third is detuning, the fourth and fifth indicate SPM and XPM terms, respectively. Here, the strengths of SPM and XPM are 1 and 2, respectively, since the medium of the resonator has little to no diffusive effect. The last term is for anomalous (normal) second-order dispersion with $\beta = 1$ ($\beta = -1$)and negative in the normal dispersion regime. In this work, we will consider no group velocity dispersion, i.e., the field envelope remains constant within a round-trip. In chapter 3, we will derive the Lugiato-Lefever equation for 1D SSH lattices that consist of ring resonators.

Figure 2.8 shows the intensities ($I_{\pm} = |E_{\pm}|^2$) in CW and CCW directions as a function of input intensity $I_s = |E_{in}|^2$ for two different values of the detuning Δ. We have plotted this figure by solving Eq. A.12 numerically for a range of input field amplitude E_{in}. It can be observed that for small detuning ($\Delta = 1.6$), CW and CCW modes propagate identically as input intensity is increased, as shown in Fig. 2.8(a). However, for detuning $\Delta = 1.85$, for example, symmetrical propagating light is followed by spontaneous symmetry breaking as depicted in Fig. 2.8(b), which is known as optical bistability. The bistability regime is limited to the values of detuning [62], which is why the symmetry broken CW and CCW modes after appearing restores the symmetry state. In the next section, we will explain sublattice symmetry and CW-CCW symmetry through the SSH lattice

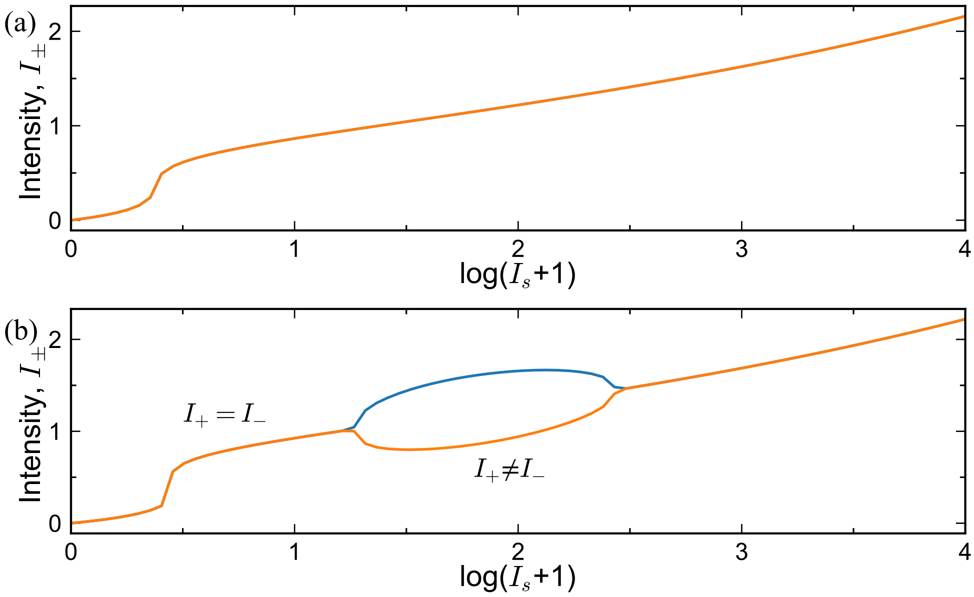

Figure 2.8: Intensities in CW (I_+) and CCW (I_-) directions as function of input intensity I_s with provided $\Delta = 1.6$ in (a) and $\Delta = 1.85$ in (b), using Eq. A.12

with the on-site Kerr effect.

2.5 Bifurcations in dynamical systems

A bifurcation is a phenomenon in nonlinear dynamical systems in which a slight change in a system's parameters leads to a significant, sudden, and qualitative shift in its behavior. It marks the transition between stable, periodic, or chaotic states. The logistic map is one of the most famous examples of a system with many bifurcations, a simple nonlinear difference equation utilized to model population growth [84]. One can write a logistic map such as:

$$x_{n+1} = rx_n(1 - x_n), \tag{2.16}$$

where x is the population at time n and r is a control parameter indicating the growth rate. Depending on the growth rate, the function of the logistic map

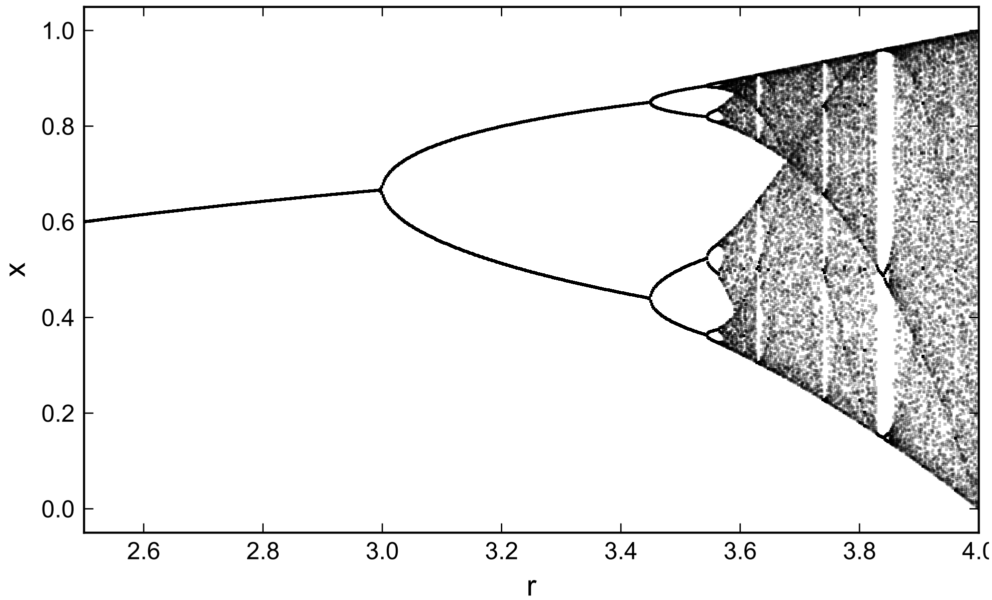

Figure 2.9: Bifurcation diagram is determined by solving Eq. 2.16.

presents different behaviors, as shown in Fig. 2.9. It converges to a stable fixed point as long as $r \leq 3$, meaning the population remains constant over time as illustrated in Fig. 2.10(a). Increasing r ($3 < r < 3.45$) leads to a sub-harmonic (or period-doubling) bifurcation where the population oscillates between two values; for example, at $r = 3.3$, the population alternates between around 0.55 and 0.84 as shown in Fig. 2.10(b). As the growth rate increases, these asymptotic state values double to four and so on, until the population becomes chaotic. Figure 2.10(d) shows an example of a chaotic population at $r = 3.9$.

2.6 Saddle-Node Bifurcation

Saddle-node bifurcation occurs when a pair of fixed points, one stable and one unstable, collide and annihilate each other as a control parameter is varied. The

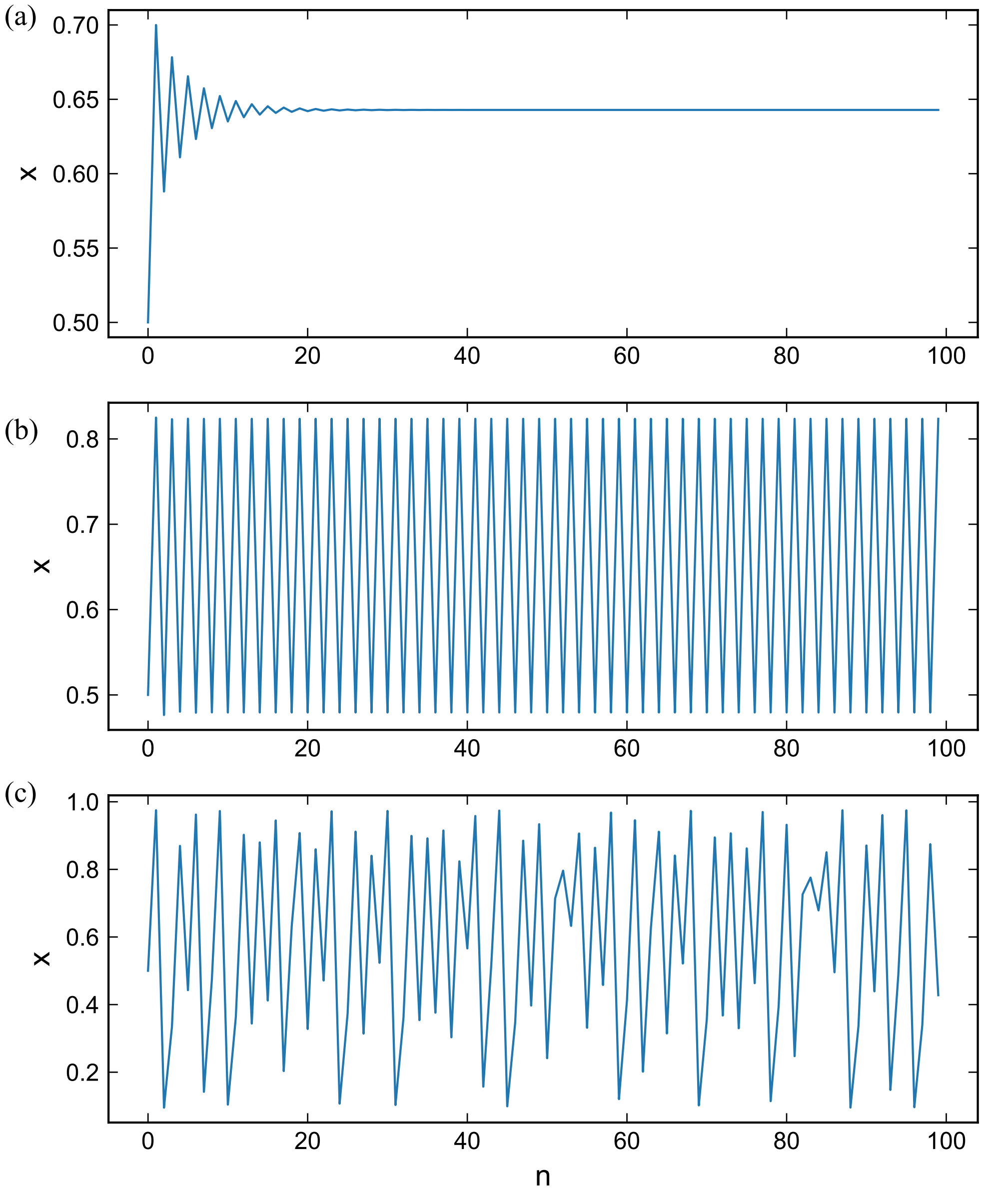

Figure 2.10: Population dynamics. (a) Fixed point, $r = 2.8$, (b) periodic oscillations, $r = 3.3$, (c) chaotic oscillations $r = 3.9$.

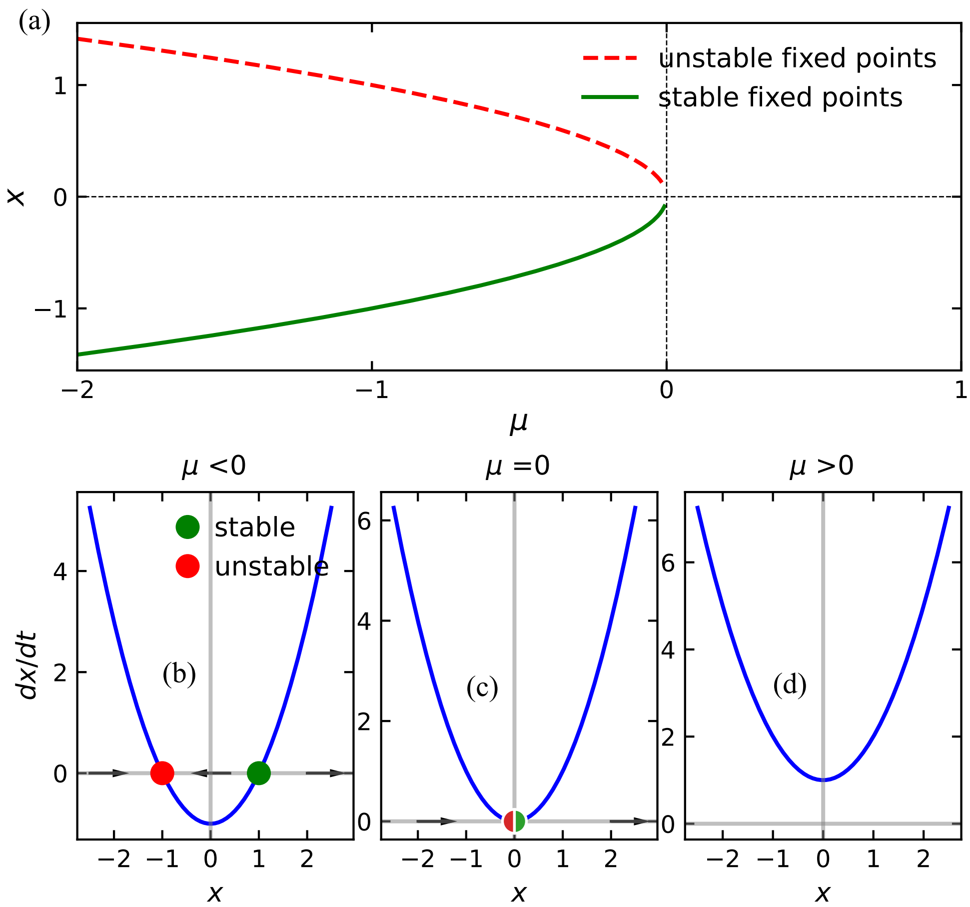

Figure 2.11: (a) Saddle-node bifurcation diagram. Flow diagrams for $\mu < 0$ in (b), $\mu = 0$ in (c) and $\mu > 0$ in (d). Arrows indicate how the solution x evolves.

normal form for a saddle-node bifurcation is:

$$\frac{dx}{dt} = \mu - x^2, \tag{2.17}$$

where μ is the bifurcation parameter. Figure 2.11(a) shows the bifurcation diagram as a function of μ. There are two fixed points when $\mu < 0$, as shown in Fig. 2.11(b). At $\mu = 0$, the fixed points combine into a semi-stable fixed point as illustrated in Fig. 2.11(c); in this case, the fixed point is called a saddle-node fixed point. This fixed point disappears once $\mu > 0$ as shown in Fig. 2.11(d).

2.7 Pitchfork bifurcation

The pitchfork bifurcation is a fundamental phenomenon in the study of nonlinear dynamical systems, often associated with the emergence of spontaneous symmetry breaking (SSB). It occurs when a symmetric system, as a control parameter is varied, transitions from having a single stable fixed point to two new stable fixed points and an unstable one at the origin, as shown in Fig. 2.12(a). This behavior reflects the system's loss of symmetry: the original symmetric state becomes unstable, and the system spontaneously selects one of the two equivalent asymmetric states. Mathematically, the simplest normal form of a supercritical pitchfork bifurcation is given by

$$\frac{dx}{dt} = \mu x - x^3, \tag{2.18}$$

where μ is the bifurcation parameter. When $\mu < 0$ and $\mu = 0$, the origin is the only stable fixed point; when $\mu > 0$, the origin becomes unstable and two new stable fixed points appear at $x = \pm\sqrt{\mu}$, as shown in Fig. 2.12(b),(c)and(d) respectively.

In this work, we will demonstrate bifurcations between CW and CCW modes through the nonlinear Kerr effect in the 1D SSH lattice. We mean the spontaneous symmetry breaking between CW and CCW modes, forming a bifurcation.

2.8 Summary

In this chapter, we have provided a theoretical framework for understanding the key concepts and phenomena underlying the work. It begins with an introduction to the one-dimensional photonic topological insulator model, focusing on

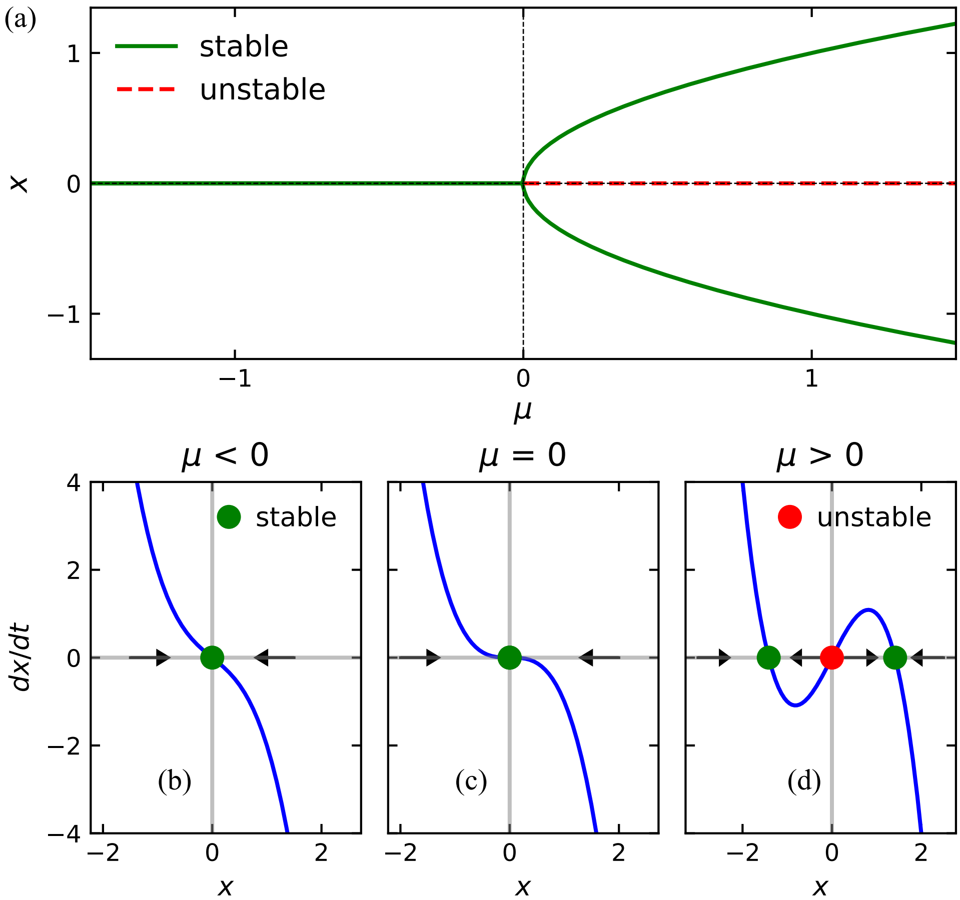

Figure 2.12: (a) Pitchfork bifurcation diagram. Flow diagrams for $\mu < 0$ in (b), $\mu = 0$ in (c) and $\mu > 0$ in (d). Arrows indicate how the solution x evolves.

the SSH Hamiltonian and its fundamental properties. The discussion highlights the emergence of edge modes as a signature of topological behavior. Then we present a brief introduction about optical ring resonator and the CROWs system. Next, the chapter shows the Kerr effect, a nonlinear optical phenomenon that introduces intensity-dependent refractive index changes that are important for symmetry-breaking mechanisms. The study of symmetry breaking in micro-ring resonators establishes a connection between nonlinear dynamics and photonic lattices. Finally, we have explained period-doubling bifurcations, saddle-node and pitchfork bifurcations in dynamical systems, providing a mathematical framework for understanding transitions in nonlinear systems. In the next chapter, we will present the first original and our significant results.

Chapter 3

1D Nonlinear Photonic Topological Insulator

This chapter is adapted from our published paper in reference [63], except for the last section.

3.1 Introduction

Nonlinear phenomena occur when the linear relationships between inputs and outputs break down, resulting in rich and complex behaviors such as bistability, where the system has two stable states for a single excitation. Optical bistability in photonic systems arises when light propagates through a cavity containing a nonlinear medium, resulting in two distinct optical states. In one state, a specific mode becomes dominant (switched on), while in the other, it is suppressed (switched off) [85]. Stable symmetry breaking has been studied in optical systems, including counter-propagating light beams in Sagnac interferometers [57], Kerr nonlinearity in microresonators [59, 62, 86–88], and one-dimensional chains of ring resonators with a one input light beam [89]. In this chapter, we will demonstrate optical bistability in a 1D nonlinear photonic topological insulator.

To better understand 1D nonlinear photonic topological insulator, we will explain briefly the linear SSH model with no resonance frequency shift first, then this model after introducing resonance frequency shift via the Kerr effect.

3.2 Linear SSH model

Here the linear 1D SSH chain consists of $(N+1)$ unit cells, with each unit cell containing two sites which belong to sublattice A and sublattice B, respectively, hosting a single ring resonator in each one as depicted in Fig. 3.1(a). However, the $(N+1)$-th unit cell has only one ring resonator, which is part of sublattice A. Consequently, there are a total of $M = 2N+1$ ring resonators in the whole system. We can control the intra- (v) and inter-cell (w)coupling coefficients by adjusting the gap size between the ring resonators. We excite the coupled ring resonators array by two optical pumps of equal intensity from one side. Both pumps are coupled into the first ring resonator but flow in opposite directions, exciting clockwise (CW) and counterclockwise (CCW) modes, respectively. The optical waves then travel throughout the resonators, moving back and forth through the couplings between each ring resonator. We apply temporal coupled mode theory [90, 91] to calculate the time evolution of field amplitudes $a_n(t)$ and $b_n(t)$ in the nth unit cell. It allows us to determine the optical intensities in CW and CCW directions. The coupled mode equations are then expressed as:

$$\frac{da_{n,\pm}}{dt} = i\Big(\omega_0 + i\gamma_n\Big)a_{n,\pm} + ivb_{n,\mp} + iwb_{n-1,\mp} + \delta_{n,1}\gamma_c s_{in},$$
$$\frac{db_{n,\pm}}{dt} = i\Big(\omega_0 + i\gamma_n'\Big)b_{n,\pm} + iva_{n,\mp} + iwa_{n+1,\mp}, \tag{3.1}$$

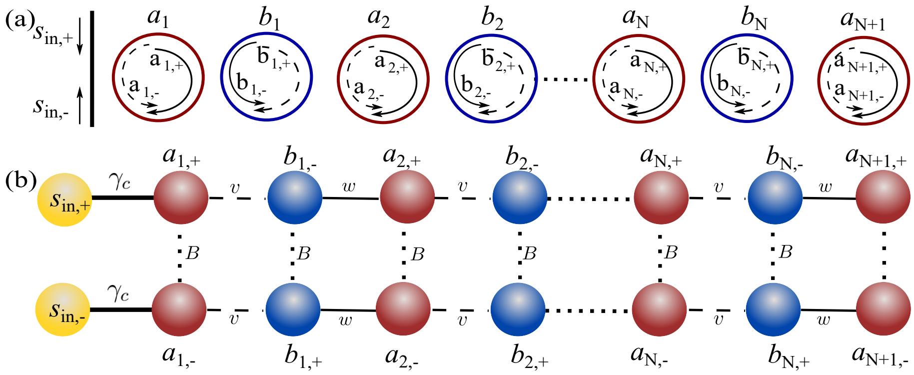

Figure 3.1: (a) A coupled ring resonators array based on SSH model with alternating gap sizes, pumped with amplitude $s_{in,\pm}$. (b) A nonlinear SSH model with XPM strength B. v and w are the inter- and intra-cell coupling coefficients, respectively, and γ_c is the coupling coefficient between the pumping source and the first ring resonator.

where

$$\begin{aligned} \gamma_n &= \gamma_0 + \delta_{n,1}\gamma_c, \\ \gamma_n' &= \gamma_0 \end{aligned} \tag{3.2}$$

where subscript $\pm$ represents the directions of propagation in CW and CCW, respectively. $\delta_{n,1}$ is the Kronecker delta function, ω_0 is the resonance frequency of the uncoupled ring resonators, and γ_0 indicates an intrinsic loss. The input beams with the same amplitude, s_{in}, are given as $\sqrt{I_s}e^{i\omega t}$. Here, the input beam couples to the two CW and CCW modes in the first ring only ($a_{1,\pm}$) with the coefficient γ_c. Only a_n's and b_n's are time-dependent functions, and the notation (t) has been omitted for simplicity. For conciseness, we will write the coupled mode equations (Eq. (3.1)) in matrix form, utilizing the Hamiltonian $\mathbf{H}$ as follows:

$$\frac{d\mathbf{x}}{dt} = \mathbf{H}\mathbf{x} + \mathbf{S} \tag{3.3}$$

where

$$\mathbf{x} = (a_{1,+}, b_{1,-}, a_{2,+}, b_{2,-}, \ldots, a_{1,-}, b_{1,+}, a_{2,-}, b_{2,+}, \ldots)^{\mathsf{T}}.$$

Note that the Hamiltonian $\mathbf{H}$ can be redefined by multiplying both sides by i, resulting in an equation that resembles the Schrödinger equation, where the eigenvalues correspond to the real parts of the frequencies. We have adopted this notation to align Eq. (3.3) with the Lugiato-Lefever equation, which we will explain in the following section. Then, the Hamiltonian $\mathbf{H}$ can be divided into two terms:

$$\mathbf{H} = \mathbf{H}_0 + \mathbf{H}_c \tag{3.4}$$

where

$$\mathbf{H}_0 = i(\omega_0 + i\gamma_0)\mathbb{I}_M \tag{3.5}$$

with $\mathbb{I}_M$ the $(M \times M)$ identity matrix. The nearest-neighbour coupling matrix, $\mathbf{H}_c$, can be expressed as:

$$\mathbf{H}_c = i \begin{pmatrix} 0 & v & 0 & 0 & \cdots \\ v & 0 & w & 0 & \cdots \\ 0 & w & 0 & v & \cdots \\ 0 & 0 & v & 0 & \cdots \\ \vdots & \vdots & \vdots & \vdots & \ddots \end{pmatrix}. \tag{3.6}$$

The last term in Eq. 3.3, the source term $\mathbf{S}$ which is expressed as

$$\mathbf{S} = [s_{in,+}, 0, 0, \cdots, s_{in,-}, 0, 0, \cdots]^{\mathsf{T}}. \tag{3.7}$$

In this work, we assume identical pumping by setting $s_{in,+} = s_{in,-}$. We can solve the coupled mode equations (Eq. (3.3)) in both frequency and time domains. In the frequency domain, assuming $\mathbf{x} = \tilde{\mathbf{x}} \exp(i\omega t)$, yields an eigenvalue equation

$$i\omega\tilde{\mathbf{x}} = \mathbf{H}\tilde{\mathbf{x}}. \tag{3.8}$$

When we solve the eigenvalue equation, we obtain a frequency spectrum that contains "zero-energy modes". These modes are localised at one edge (the first or the last site) which has a link to the neighbour site with a smaller coupling coefficient among v and w. For example, the modes are localised at the site a_1 if $v < w$ and the site a_{N+1} if $v > w$ in Fig. 3.1. In this work, we refer to these modes as *edge modes* rather than zero edge modes, as their frequencies deviate from the resonance frequency ω_0, making them no longer zero-energy modes in nonlinear scenarios. We term the remaining modes as *bulk modes*, as their mode fields are distributed across the entire SSH lattice.

3.3 Nonlinear SSH model

Now, we consider the couplings between the CW and CCW modes due to the Kerr nonlinearity. The Kerr nonlinearity induces several nonlinear effects but here, we only consider the SPM and XPM of the ring resonators, which lead to a shift of the resonance frequencies of CW or CCW modes. In Fig. 3.1(b), only the XPM is shown, but the frequency shifts $\Delta\omega$ is given by $(I_+ + 2I_-)$ where I_+ and I_- are the intensities of the CW and CCW modes in the ring resonators. In Figure 1(b), only the couplings caused by the XPM are displayed. However, the frequency shift can be defined as the sum of $(AI_{n,+} + BI_{n,-})$, where $I_{n,+}$ and $I_{n,-}$ represent the intensities of the clockwise and counterclockwise modes in the nth ring resonator, respectively. A and B are the strength coefficients for SPM and XPM, respectively. For simplicity, we describe the field amplitudes in our nonlinear SSH model using the normalized Lugiato-Lefever equation [85].

Consider $\tilde{a}(t)$ and $\tilde{b}(t)$ represent the time-varying envelope amplitudes, where $a(t) = \tilde{a}(t)e^{i\omega t}$ and $b(t) = \tilde{b}(t)e^{i\omega t}$, the Lugiato-Lefever equation for a 1D SSH array of nonlinear ring resonators can then be written as:

$$\begin{aligned}
\frac{d\tilde{a}_{n,\pm}}{d\bar{t}} &= -\tilde{a}_{n,\pm} - i\Delta\tilde{a}_{n,\pm} + i\eta(A|\tilde{a}_{n,\pm}|^2 + B|\tilde{a}_{n,\mp}|^2)\tilde{a}_{n,\pm} + iv\tilde{b}_{n\mp} \\
&\quad + iw\tilde{b}_{n-1,\mp} + \delta_{n,1}\gamma_c s_{in}, \\
\frac{d\tilde{b}_{n,\pm}}{d\bar{t}} &= -\tilde{b}_{n,\pm} - i\Delta\tilde{b}_{n,\pm} + i\eta(A|\tilde{b}_{n,\pm}|^2 + B|\tilde{b}_{n,\mp}|^2)\tilde{b}_{n,\pm} + iv\tilde{a}_{n\mp} \\
&\quad + iw\tilde{a}_{n+1,\mp},
\end{aligned} \tag{3.9}$$

where $\bar{t}$ is the dimensionless time, $\bar{t} = t\gamma_0$. The first term on the right-hand side represents damping, while the second term corresponds to normalized detuning ($\Delta = (\omega - \omega_0)/\gamma_0$), which is the difference between the input continuous wave frequency and the resonance frequency of an individual ring resonator. The third and fourth terms represent SPM and XPM, respectively, with the normalized nonlinear coefficients A and B. Here, $\eta = +1$ indicates a self-focusing medium, while $\eta = -1$ indicates a self-defocusing medium. The terms involving v and w represent the intra- and inter-couplings between the ring resonators, similar to the linear case. Finally, we introduce a nonlinear term into Eq. (3.4) to obtain the Hamiltonian for our nonlinear SSH model:

$$\mathbf{H} = \mathbf{H}_0 + \mathbf{H}_c + \mathbf{H}_{NL}, \tag{3.10}$$

where

$$\mathbf{H}_0 = -(1 + i\Delta)\mathbb{I}_{2M}, \tag{3.11}$$

and

$$\mathbf{H}_{NL} = i\eta \mathbb{I}_{2M} \times \mathbf{diag}\left(\delta_{1,a}^{cw}, \quad \delta_{1,b}^{cw}, \quad \ldots, \quad \delta_{1,a}^{ccw}, \quad \delta_{1,b}^{ccw}, \quad \ldots \right). \tag{3.12}$$

Here $\delta_{n,a}^{cw}$ and $\delta_{n,a}^{ccw}$ are, respectively, defined as:

$$\delta_{n,a}^{cw} = A|\tilde{a}_{n,+}|^2 + B|\tilde{a}_{n,-}|^2,$$

and

$$\delta_{n,a}^{ccw} = A|\tilde{a}_{n,-}|^2 + B|\tilde{a}_{n,+}|^2.$$

Similarly we can define $\delta_{n,b}^{cw}$ and $\delta_{n,b}^{ccw}$.

Due to nonlinear terms, we cannot convert Eq.(3.3), which is the time-dependent equation, into an eigenvalue equation. Therefore, we will determine the temporal evolution of the amplitudes $\tilde{a}_{n,\pm}$ and $\tilde{b}_{n,\pm}$ numerically, using the Runge-Kutta fourth-order method.

3.4 Optical bistabilty

As we have seen in chapter two, that section 2.2, the Kerr effect causes optical bistability.

To theoretically investigate optical bistability in the nonlinear SSH lattice, we consider an SSH array comprising seven ring resonators ($M = 7$). The system is characterized by a detuning parameter Δ set to 1.85, with the nonlinear coupling strengths defined as $A = 1$ and $B = 2.5$. We use alternating coupling coefficients $v = 3$ and $w = 7$. In our simulations, we varied the pump intensity I_s within a specific range, initializing the system with random initial conditions. As illustrated in Fig. 3.2(a), optical bistability is observed, the balance between

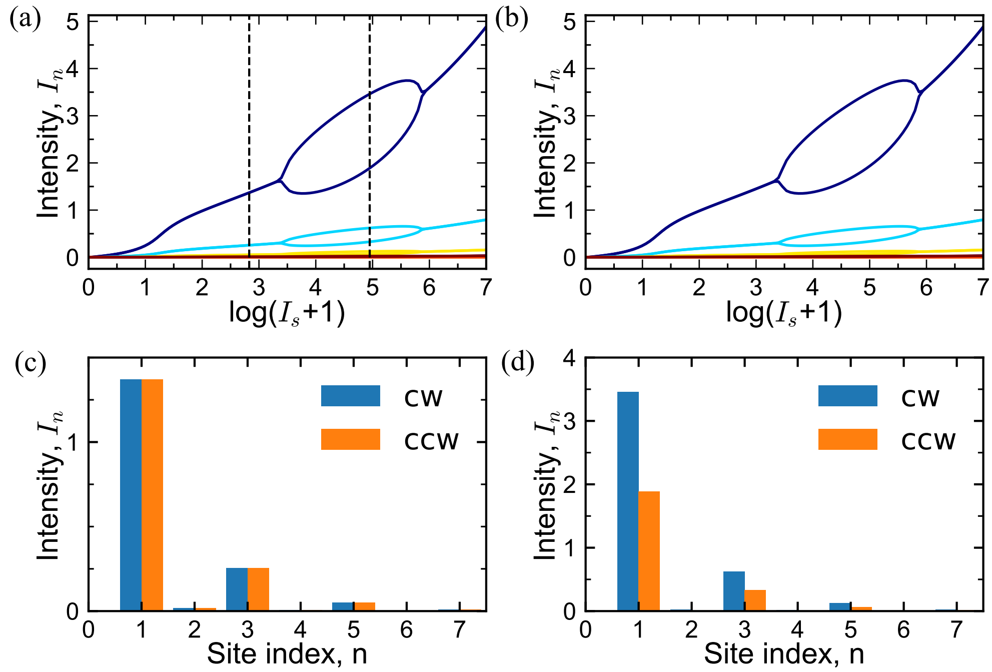

Figure 3.2: Optical bistability for SSH lattice, $M = 7$, $v = 3$, $w = 7$, $\gamma_c = 0.01$ and $\Delta = 1.85$ with Kerr nonlinearity in each resonator(a) while only in the first resonator in (b). (c), (d) The intensity distributions corresponding to the input intensities indicated by the dashed vertical lines in panel (a).

the clockwise (CW) and counterclockwise (CCW) modes is disrupted within the pump intensity range of $\log(I_s + 1) = 3.5$ to $\log(I_s + 1) = 5.8$. In this range, one of the modes (either CW or CCW) becomes stronger while the other mode is suppressed.

Figures 3.2(c) and 3.2(d) show that the intensity decreases steadily toward the center of the lattice system. Notably, the intensity is relatively large only at the odd sites (sublattice A), and the intensity exhibits an exponential decay along the right direction in both the single-stable [Fig. 3.2(c)] and bistable cases [Fig. 3.2(d)], reminiscent of the zero-energy edge modes.

To provide a clearer understanding of the observed optical bistability, we hypothesize that this phenomenon originates from symmetry breaking occurring specifically within the first ring resonator. In a single-ring resonator case, optical bistability is achieved when the pump intensity is above a critical threshold known as the bifurcation point. Consequently, it is expected that the first ring will be the first one to demonstrate optical bistability as we gradually increase the pump intensity, especially when the excitation is near the zero-energy frequency. Notably, the detuning value of 2.1 is significantly smaller than the topological band gap, calculated as $2|v - w|$, which equals 8. It means that even when the system is off-resonance, the zero-energy edge mode remains dominantly excited. This is supported by the field intensity distribution shown in Fig. 3.2(d). Since the intensities in the remaining rings are significantly lower than that of the first ring, bistability is introduced solely by the first ring. The modes within the first ring sequentially couple to the other rings, rather than generating additional optical bistability from the subsequent rings. To further verify this propagation of asymmetric intensities, we apply the Kerr effect exclusively to the first ring resonator while keeping all other parameters unchanged. As shown in Fig. 3.2(b), the resulting intensity curve closely matches the original (Fig. 3.2(a)), with only a slight decrease in the I_s range and a minor alteration in the intensity difference between the two counterpropagating modes.

3.5 Nonlinear SSH lattice with bidirectional pumping from the ends

Now, we consider a situation when the SSH lattice consisting of identical Kerr ring resonators is pumped by four sources, as illustrated in Fig. 3.3. The sources are placed on the right and left of the SSH lattice, two on each side. All the input lasers are identical, i.e. they have identical field amplitudes and frequencies. Then, the Lugiato-Lefever equations are similar to Eqs. (A.12); the difference is to add the source term for the equation describing the end ring resonator. Then they can be written as:

$$\begin{aligned}
\frac{d\tilde{a}_{n,\pm}}{d\bar{t}} &= -\tilde{a}_{n,\pm} - i\Delta\tilde{a}_{n,\pm} + i\eta(A|\tilde{a}_{n,\pm}|^2 + B|\tilde{a}_{n,\mp}|^2)\tilde{a}_{n,\pm} + iv\tilde{b}_{n\mp} \\
&\quad + iw\tilde{b}_{n-1,\mp} + \delta_{l,l}s_{in}, \\
\frac{d\tilde{b}_{n,\pm}}{d\bar{t}} &= -\tilde{b}_{n,\pm} - i\Delta\tilde{b}_{n,\pm} + i\eta(A|\tilde{b}_{n,\pm}|^2 + B|\tilde{b}_{n,\mp}|^2)\tilde{b}_{n,\pm} + iv\tilde{a}_{n\mp} \\
&\quad + iw\tilde{a}_{n+1,\mp},
\end{aligned} \tag{3.13}$$

where subscript $l = [1, N+1]$ for only sub-lattice B.

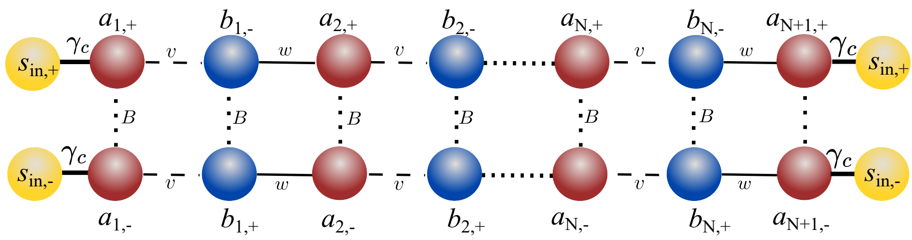

Figure 3.3: Schematic of nonlinear SSH with sources at the ends.

Figure. 3.4 (a) shows the intensity for the SSH lattice comprising seven ring resonators. For low input intensity, it can be observed that the circulating intensity in CW and CCW directions in each ring resonator propagates symmetrically, but the first ring resonator has the largest intensities. However, when the input intensities are increased further, the intensity in the sixth resonator grows significantly, crossing the intensity in the third ring resonator. Close to the crossing point, we can observe spontaneous symmetry-breaking between CW and CCW intensities in odd sites. By tuning the coupling coefficients, when setting coupling strength to smaller values ($v = 0.3$, $w = 0.7$), the intensity is concentrated at the ends of the SSH lattice as depicted in Fig. 3.4(b) and 3.4(d). In addition, tuning the coupling confines spontaneous symmetry-breaking to the first ring resonators.

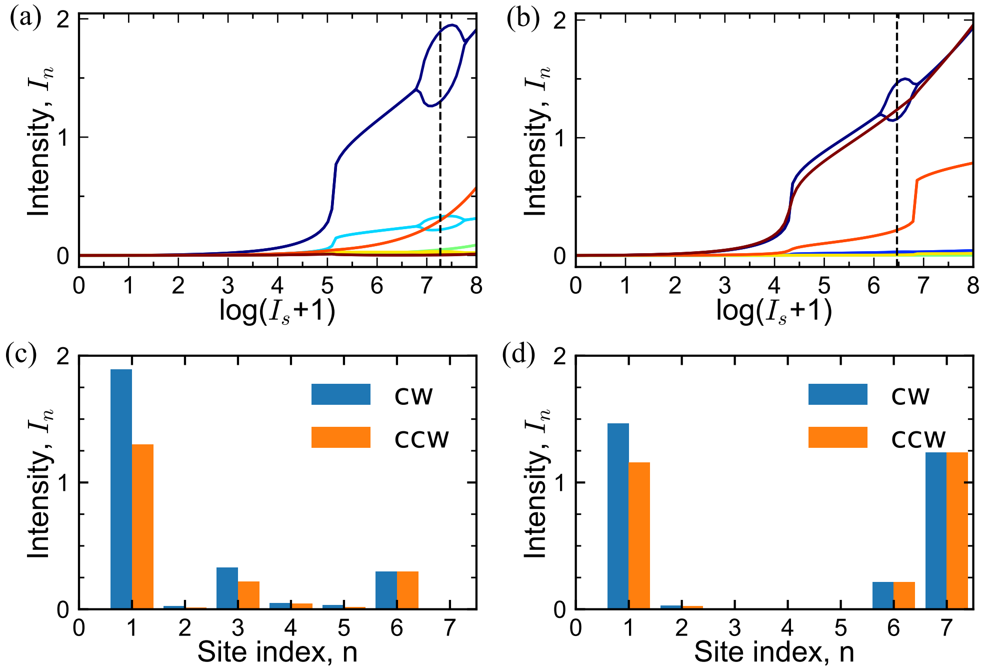

Figure 3.4: Optical bistability from solving Eq. (3.13) for 7 ring resonators, $\Delta = 2, \gamma_c = 0.1, A = 1$ and $B = 2$. (a)$v = 3$ and $w = 7$. (b)$v = 0.3$ and $w = 0.7$. (c) The intensity distribution at $log\ (I_s + 1) = 7.3$ in (a). (d) The intensity distribution at $log\ (I_s + 1) = 6.5$ in (b).

3.6 Summary

In this chapter, we have extended the Lugiato-Lefever model to describe field amplitudes in a 1D SSH lattice composed of ring resonators exhibiting Kerr nonlinearity. We have solved Lugiato-Lefever equations numerically using a fourth-order Runge-Kutta method. When nonlinear terms are included in the Lugiato-Lefever equation, we observed that the CW and CCW mode intensities in the first ring remain symmetric until the pump intensity reaches a critical bifurcation point. Beyond this threshold, symmetry breaks spontaneously as the resonance frequencies of the CW and CCW modes in the first ring resonator begin to split. In addition, we have added more sources to pump the nonlinear SSH lattice from both sides symmetrically, still capable of showing the optical bistability. In this chapter, we have set the XPM constant to 2 and 2.5. In the next chapter, we will consider larger B values to show a different behavior: periodic and chaotic oscillations.

Chapter 4

Complex light propagation in the 1D Su-Schrieffer-Heeger model

This chapter is adapted from the published paper in reference [63].

4.1 Introduction

In the previous chapter, we examined the phenomenon of optical bistability under the influence of a small XPM strength. This time, we will delve into more intricate behaviors that emerge when the XPM strength is significantly increased, accompanied by a high input pump intensity and considerable detuning. By exploring these conditions, we aim to investigate the rich dynamics and complexities that arise in the nonlinear SSH lattice.

4.2 Oscillation phases

Now, let us delve into the temporal evolution of optical intensities within a 1D SSH array comprising seven ring resonators. To investigate the periodic oscillation and chaotic phases present in our nonlinear system, we will generate a Poincaré section by plotting all the local maxima from the time series of oscillating intensities. Figure 4.1 shows Poincaré sections of maxima intensity for each site in the nonlinear SSH lattice, grouping into odd (Figure 4.1(a)) and even sites (Figure 4.1(b)). It is obvious that each ring resonator located at an odd site (sublattice A) has similar phases, including bistability and oscillations. As the intensity patterns of each ring in the 1D SSH array closely follow that of the first ring, we will focus on plotting the Poincaré sections for the first ring resonator. This approach will deepen our understanding of the system's dynamics.

To observe how the input intensity can affect the temporal dynamic of the nonlinear SSH lattice, we plot the Poincaré section at low and high input intensity as shown in Figs. 4.2(a) and 4.2(b), respectively. We scan the detuning across the full spectral range encompassing the edge state and all bulk modes with both negative and positive detuning in the linear SSH lattice, as indicated by the vertical dashed lines in the figures. In this analysis, we set $A = 1$ and $B = 4$, varying the pump intensity from 0.05 to 40 as indicated by different colors. As illustrated in the zoomed view of the plots, seven modes account for edge and bulk modes. The edge mode shows the highest intensity in the center of the spectra, with six bulk modes situated on both sides of the edge mode, three on each side. At low pump intensities, as shown in Fig. 4.2(a), the edge mode experiences a significant shift towards larger detuning values and its intensity increases markedly. In contrast, the bulk modes shift less noticeably with a slight increase in intensities. This behavior can be attributed to the concentration of light intensity in the first ring resonator. Under conditions of high pump intensity, as illustrated in Fig. 4.2(b), the CW and CCW modes of the edge mode experience a significant interaction caused by XPM. It leads to

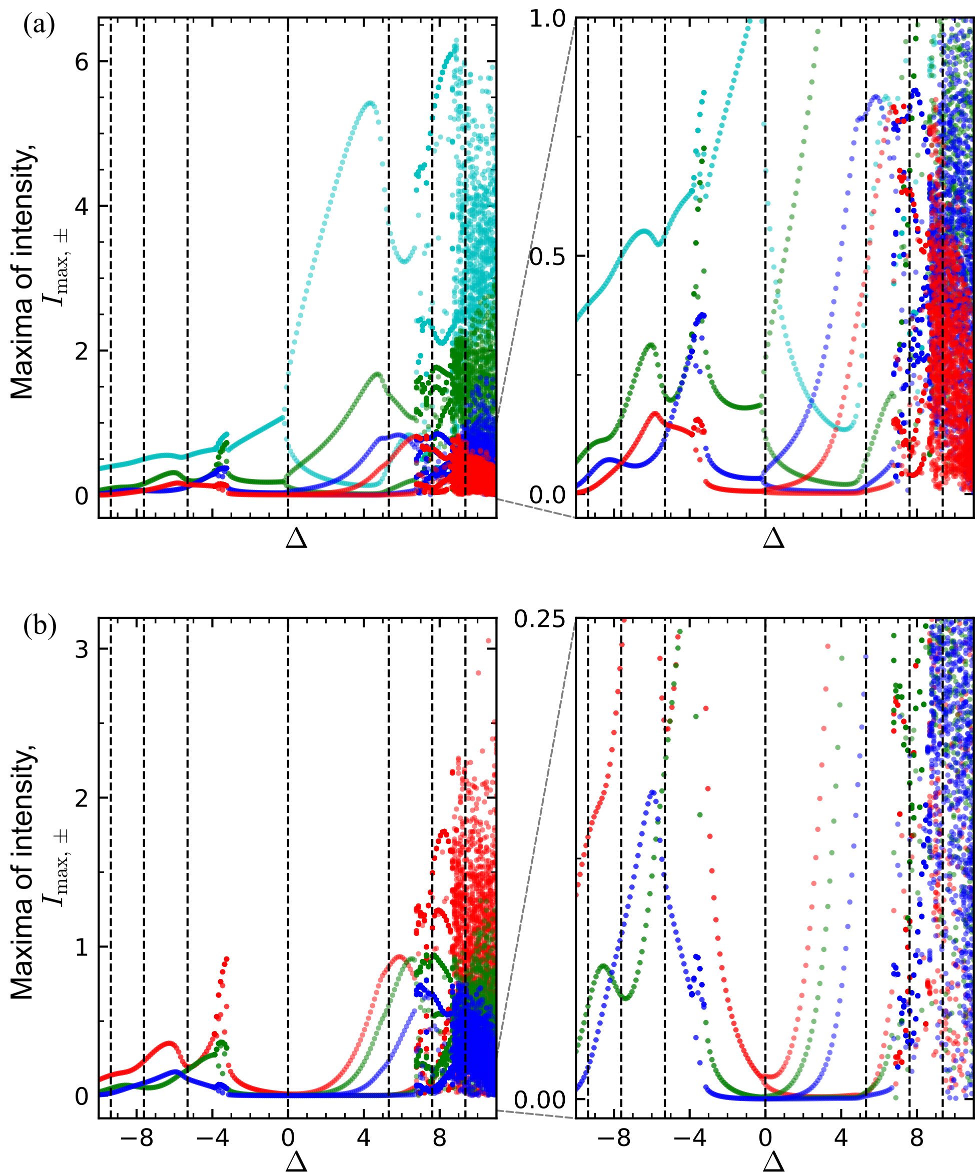

Figure 4.1: Poincaré sections of the maxima of oscillating coupled intensity as a function of detuning for a 1D SSH lattice ($M = 7$) with $I_s = 40, v = 3, w = 7, A = 1, B = 4$. (a) For odd sites with the cyan, green, blue, and red colors corresponding to the 1st, 3rd, 5th, and 7th ring resonators, respectively. (b) For even sites with the red, green, and blue colors corresponding to the 2nd, 4th, and 6th ring resonators, respectively.

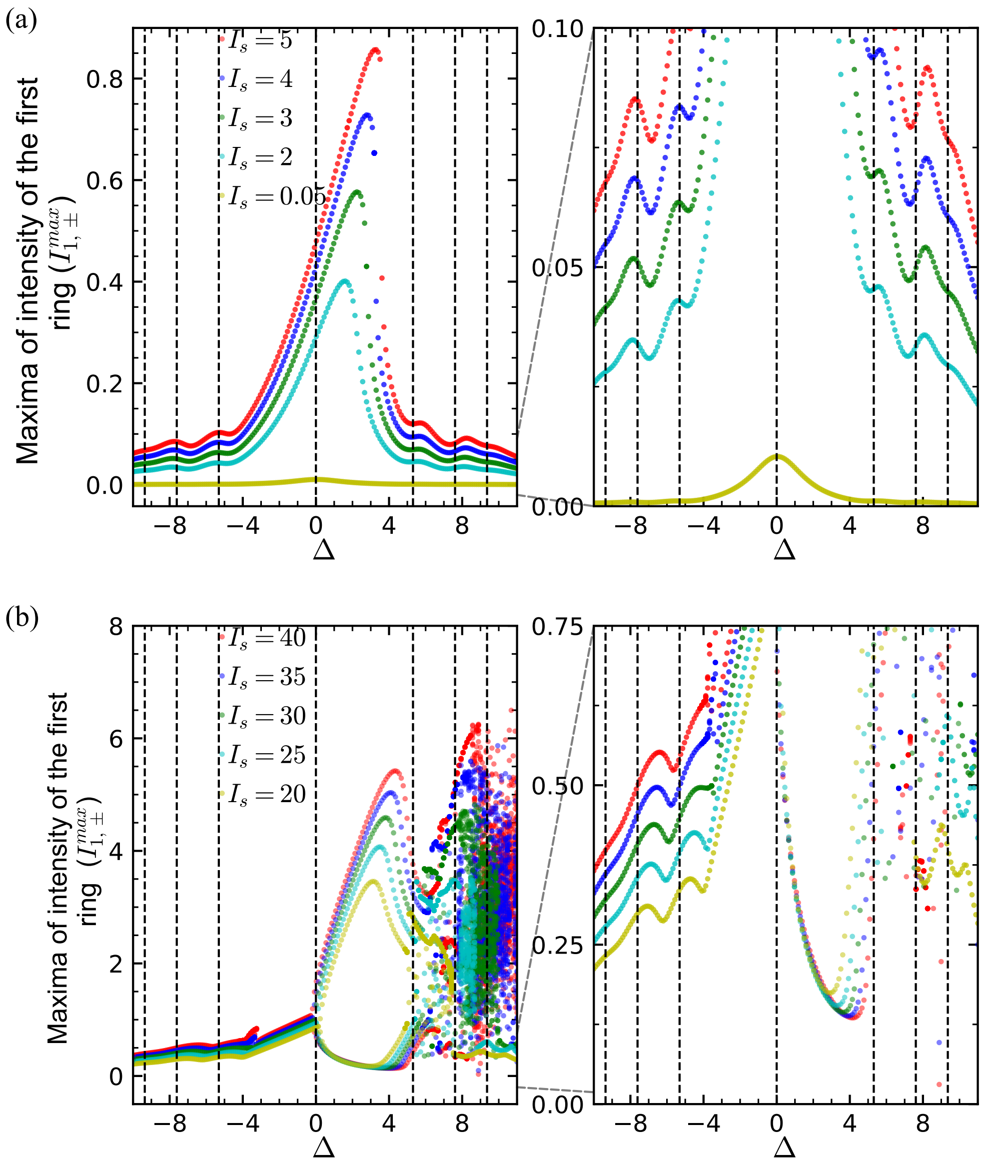

Figure 4.2: The Poincaré section displays the maxima of the CW and CCW intensity time series for the first ring resonator in a 1D SSH lattice consisting of seven ring resonators with $v = 3$, $w = 7$, $A = 1$, and $B = 4$. (a) Shows the maximum intensity curves at low input intensities I_s. (b) For high input intensities I_s, both optical bistability and oscillation regions emerge. Vertical dashed lines represent frequencies derived from the eigenvalue equation Eq.(3.8) for the linear case.

a rise in optical bistability. Furthermore, increasing pump intensity creates a notable overlapping between the edge mode and the bulk mode near $\Delta = 6.8$ when $I_s = 40$, resulting in a series of oscillation phases for both clockwise CW and counterclockwise CCW modes as illustrated in Fig 4.3(a). It is important to note that the CW and CCW intensities can be exchanged at any time for bistable and oscillation phases. This is because the chirality of the system depends on its historical dynamics, which, in our case, is determined by the initial conditions. Similar behaviors have been observed in experimental and theoretical works of the counter-propagating in a single ring resonator [58, 60, 62, 83, 92].

4.3 Asymmetry for CW and CCW modes

To quantify the extent of symmetry breaking between clockwise CW and CCW modes (see section B), we define an asymmetry parameter, following an approach similar to that used for a single microcavity in Ref.[93]. It can be expressed as:

$$D = \frac{\sum_n I_{CW,n} - \sum_n I_{CCW,n}}{\sum_n I_{CW,n} + \sum_n I_{CCW,n}}. \tag{4.1}$$

A positive value of D signifies that the CW mode has a greater influence or strength compared to the CCW mode. In contrast, a negative value of D indicates that the CCW mode is dominant over the CW mode. When D is equal to zero, meaning that both modes are balanced and exhibit symmetry. In the bistability regime, the nonlinear system demonstrates a relatively large asymmetry close to 1, as illustrated in Fig. 4.3(b). It indicates a significant breaking of the CW-CCW symmetry. In contrast, in the oscillations regime when $\Delta > 6.9$ the asymmetry becomes highly sensitive to detuning, fluctuating randomly between -1 and 1. A similar pattern is observed in the asymmetry spectrum calculated specifically for the first ring, confirming that the optical bistability primarily arises in the nonlinear SSH lattice from the bifurcation of CW and CCW modes in this first ring.

4.4 Polarization

To investigate the breaking of sublattice symmetry (as discussed in section B), we calculate the polarization P based on $\sum_n I_{A,n}$ for sublattice A and $\sum_n I_{B,n}$ for sublattice B. The polarization for each direction is determined using the equation:

$$P = \frac{\sum_n I_{A,n} - \sum_n I_{B,n}}{\sum_n I_{A,n} + \sum_n I_{B,n}}. \tag{4.2}$$

In Fig. 4.3(c), the CW and CCW modes within the bistability regime exhibit positive polarization values. The polarization with values close to 1 refers to the localization of intensity in sublattices A. In other words, the energy of the modes at A sites is concentrated. This reflects the topological zero-energy mode, which exhibits a completely polarized distribution, meaning that $P = 1$.

4.5 Participation ratio

To better understand how the intensity of dynamic modes is localized across the nonlinear SSH lattice, we compute the participation ratio PR [94]. By analyzing the PR, we can gain insights into the distribution of dynamic modes within the lattice structure. It is written as

$$PR = \frac{(\sum_n I_n)^2}{\sum_n I_n^2}. \tag{4.3}$$

The participation ratio with large value $PR > 1$ ($PR = 1$) signifies delocalization (localization) within the system. When the detuning values are small ($\Delta \leq 1.9$), as illustrated in Fig. 4.3(d), both CW and CCW modes exhibit almost identical participation ratios. However, as the detuning increases (when $\Delta > 1.9$), a distinct change occurs; one of the modes—either CW or CCW—becomes significantly more localized than the other.

4.6 Spatiotemporal distribution

To enhance the understanding of the asymmetrical dynamic modes, we analyze the spatial distributions and temporal variations of the excited mode intensity across different detuning values, as illustrated in Fig. 4.4 and Fig. 4.5, respectively. For this analysis, we specifically examine the case where the pump intensity $I_s = 40$. In the case of optical bistability ($\Delta = 4.77$), as illustrated in Figs. 4.4(a) and 4.4(b), both the CW and CCW modes exhibit contrasting intensity values. However, their intensity profiles resemble the zero-energy edge mode profile found in a linear SSH model, characterized by exponentially decaying nonzero intensities on odd sites and zero intensities on even sites. The deviations can be caused by the off-resonance excitation and the nonlinear interaction (XPM) between CW and CCW modes. It is obvious the excited mode remains stable, with constant intensities that manifest as two distinct points in phase space in Fig. 4.5 (a) and 4.5(b). As detuning is further increased to $\Delta = 7.3$, both the CW and CCW mode profiles shift away from the zero-energy edge mode. However, the CCW mode profile shows less deviation, maintaining low intensities at the even sites as shown in Figs. 4.4(c) and 4.4(d). The largest value is associated with the zero-energy edge mode at the first site. This is due to the excitation of the ring resonators from the left side by the waveguide. The

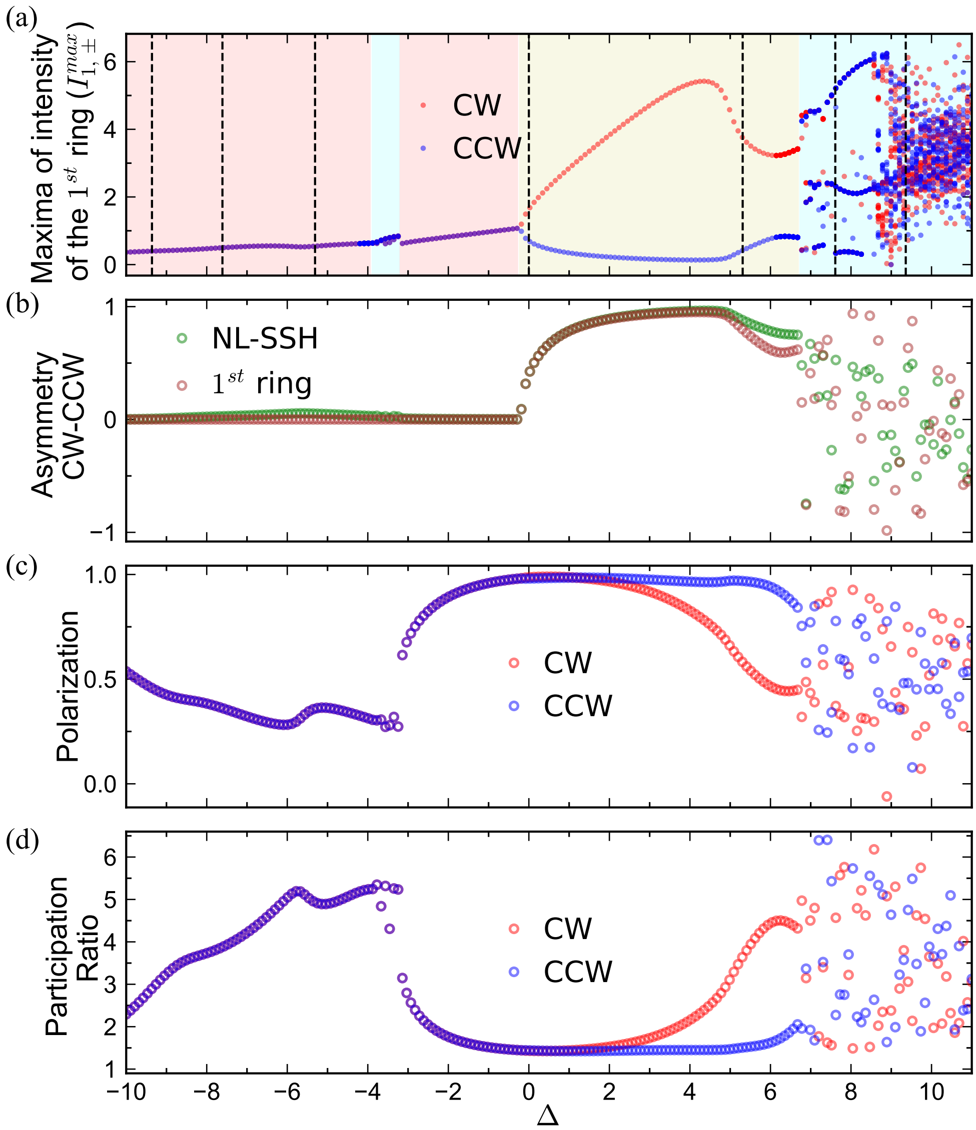

Figure 4.3: (a) Poincaré section of the maxima of intensity in the CW and CCW directions at the first ring resonator in a 1D SSH lattice, applying the same parameters' values in Fig. 4.2(b) for $I_s = 40$. Red, yellow, and cyan shading colors, respectively, point asymmetric, optical bistability, and oscillation cases. The vertical dashed lines refer to resonance frequencies for the linear 1D SSH lattice. (b) Dissymmetry between CW and CCW modes. (c) polarization in A and B sites. (d) Participation ratio for intensity.

dynamics associated with this detuning, as illustrated in Figs. 4.5 (c) and 4.5(d), exhibit periodic oscillation, resulting in the phase space being split into two distinct regions. This separation indicates that the CW mode intensity is higher

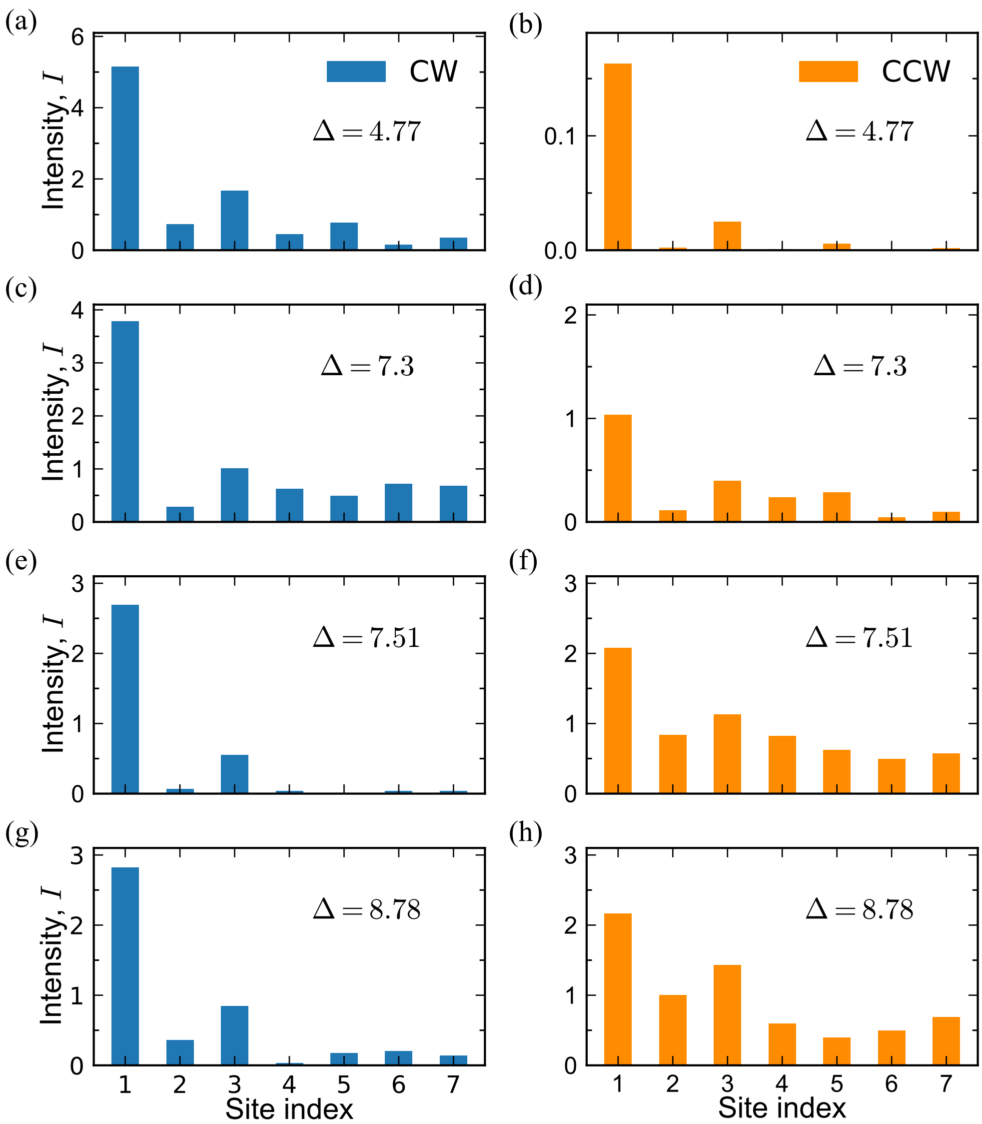

Figure 4.4: Snapshots of the intensity distribution in 1D SSH lattice with Kerr effect for the CW modes in the left column and the CCW modes in the right column for different values of detuning with $I_s = 40$, $B = 4$.

than the CCW mode intensity; the CW trajectory is positioned farther from the origin. When the detuning is slightly larger, at $\Delta = 7.51$, the two distinct trajectories converge into a single path, and the intensities switch between the CW and CCW modes [92]. They appear in different points with a π phase difference in the same phase space. On the other hand, when the detuning is larger, at $\Delta = 8.78$ as shown in Figs. 4.5(g) and 4.5(h), the system exhibits chaotic oscillations. These oscillations manifest as two distinct trajectories overlapping within a comparable phase space region.

Our analysis shows that the nonlinear SSH lattice of optical rings exhibits a series of bifurcations, chaotic dynamics, and periodic behaviors. These features strongly resemble those observed in nonlinear single-ring resonator systems [58, 60, 92], suggesting that both may share fundamental nonlinear mechanisms.

4.7 Summary

This chapter explores the intriguing oscillating behaviors observed in a nonlinear optical system, specifically employing a strong XPM strength. Our analysis focuses on seven-ring resonators, which are pumped by two laser beams positioned on one side of the structure. To illustrate the different types of oscillations present, we generated the Poincaré section, which plots the maxima of intensity in both the CW and CCW modes in relation to detuning at various levels of input power. When the input power is increased, the nonlinear SSH lattice demonstrates remarkable optical bistability, where the system can exist in two stable states alongside exhibiting oscillatory behaviors. The optical bistability is linked to edge modes, whereas the oscillations are attributed to bulk modes within the lattice. Furthermore, we conducted calculations to assess the asymmetry between the CW and CCW intensities, by examining the polarization

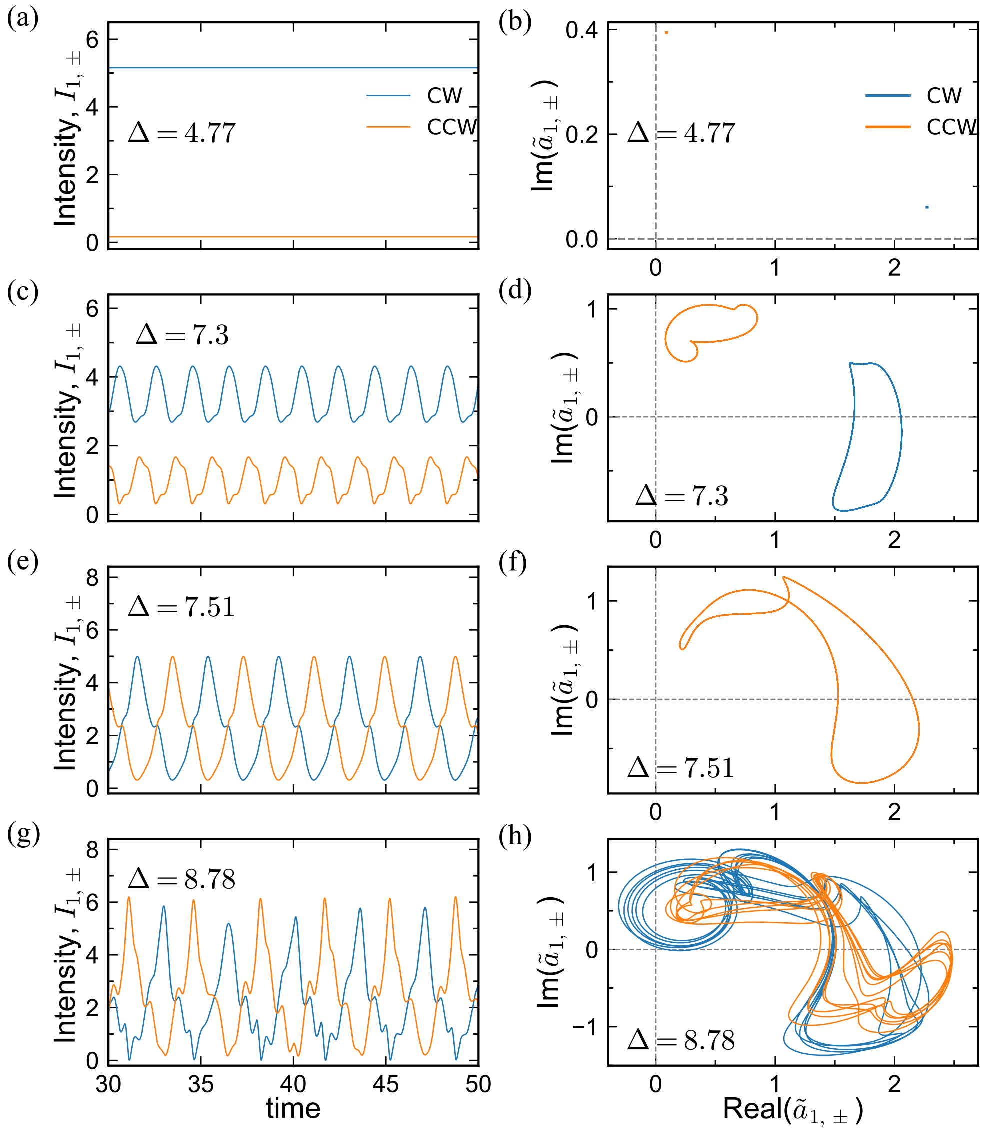

Figure 4.5: The temporal evolutions of CW and CCW modes and phase space orbits of the real and imaginary parts of field amplitude in CW and CCW direction with $A = 1$, $B = 4$ and $I_s = 40$ for the first ring resonators from 1 D SSH array of 7 rings. (a), (b) Optical bistability phase with $\Delta = 4.77$. (c), (d) Oscillations without overlapping orbits. (e), (f) Periodic switching for $\Delta = 7.51$. (g), (h) Chaotic oscillations with $\Delta = 8.87$

characteristics within sublattice A and B sites, and evaluated the participation ratio for the intensity distribution. These analyses help deepen our understanding of the dynamic of nonlinear SSH lattice and reveal the complex interplay between different modes.

Chapter 5

Dynamic phases and dynamical mode decomposition analysis for 1D nonlinear SSH lattice

5.1 Introduction

In this chapter, we will present a more in-depth analysis of our results from the previous chapter. First, we will determine the phase diagram, showing symmetry and asymmetry between CW and CCW modes. We also analyze the nonlinear SSH lattice for the case of $v = w$ and compare these findings with the case where $v \neq w$. Through this comparison, we examine the impact of the coupling coefficients on stable, bistable and oscillatory behaviors. Additionally, polarization and localization will be investigated.

Second, we will apply a data-driven technique that uses a dynamical mode decomposition DMD. By applying DMD, we can extract dominant modes and their growth rates. This method has been utilized to draw phase diagrams of topological lasing modes in SSH lattice [95].

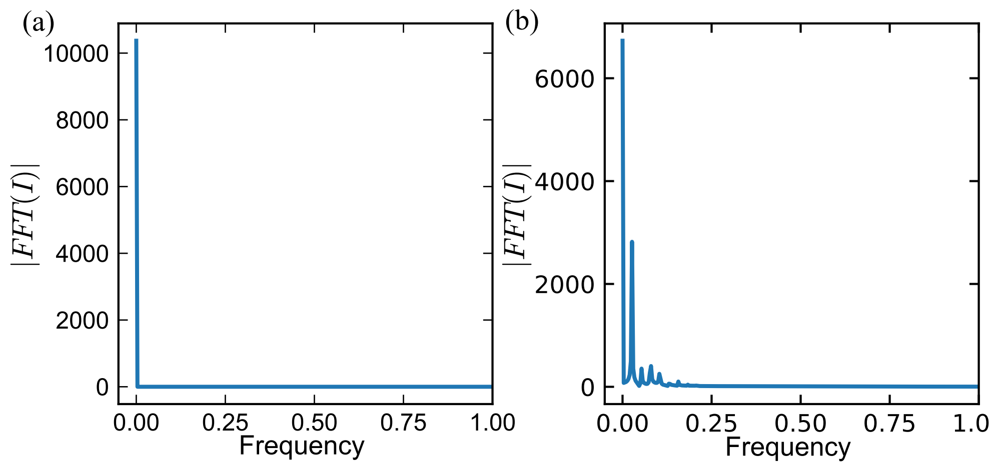

Figure 5.1: FFT spectra with $I_s = 40$, for bistability with $\Delta = 1.6$ in (a) and oscillation with $\Delta = 6.88$ in (b).

5.2 Phase diagram

To gain a deeper understanding, we have computed Eq. (3.9) for SSH lattice with seven ring resonators for a range of detuning with a range of parameters: input intensity I_s, XPM strength B, intercell coefficient w and coupling strength with source γ_c. The phase diagram has been obtained from these results using a fast Fourier transform (FFT). In this analysis, an oscillating mode is identified based on the presence of a non-zero frequency component in the FFT spectrum. Specifically, a mode is classified as oscillatory if the second-largest peak exhibits a finite value. This criterion effectively distinguishes oscillatory dynamics from stationary behavior, as shown in Fig. 5.1.

We have plotted the phase diagrams as presented in Fig. 5.2, showing different dynamics when varying the detuning with different parameters. The white horizontal dashed lines indicate the value of parameters that we have applied in chapter 4. Here, we plot phase diagrams for the first ring resonator as the patterns of other rings follow the dynamic of the first one.

Figure 5.2(a) illustrates the phase diagram as a function of detuning (Δ) and

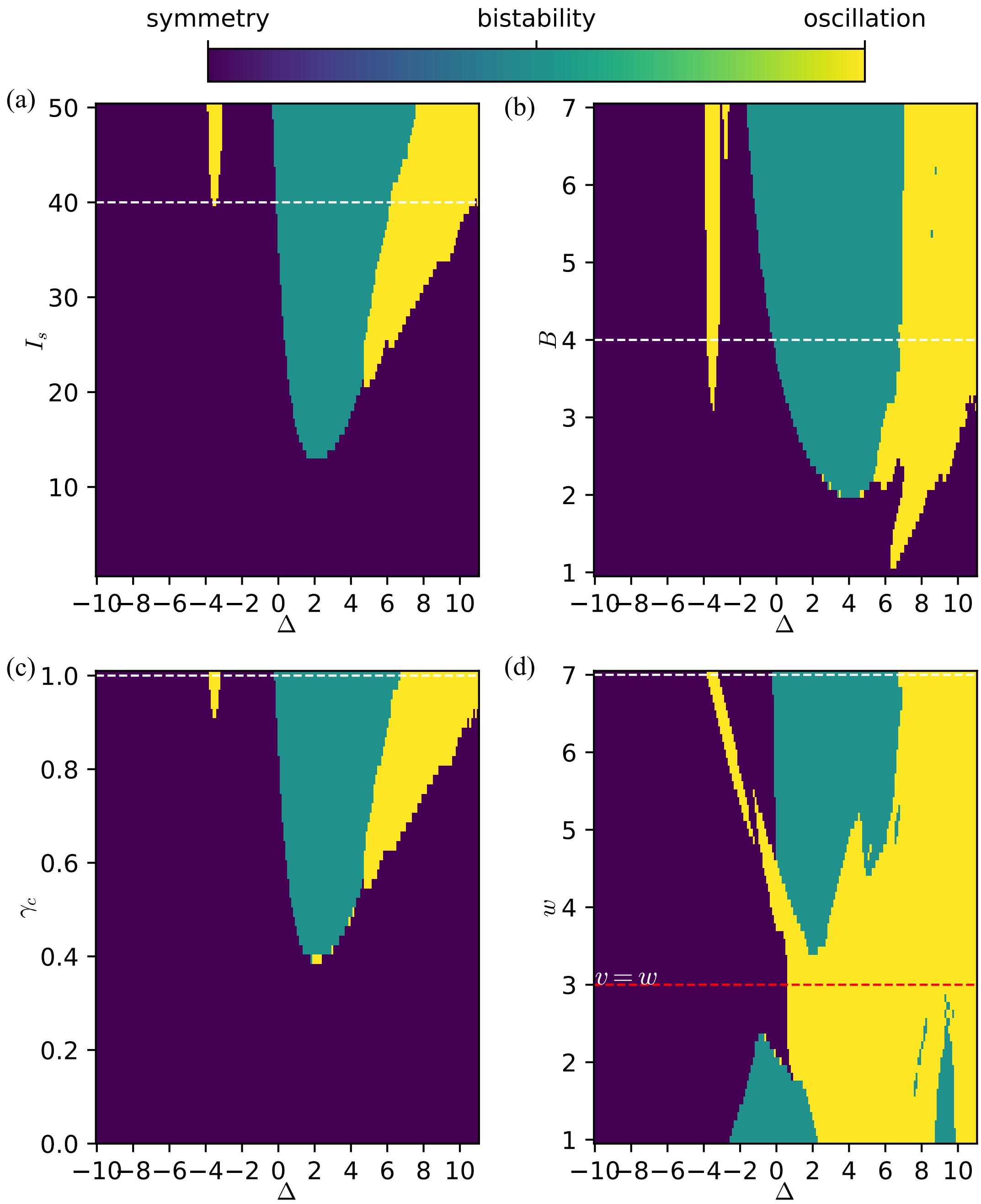

Figure 5.2: Phase diagram is obtained by applying FFT to results which we have determined from Eqs. (3.9). (a) scanning both Δ and I_s (b)scanning both Δ and B, (c) scanning both Δ and γ_c, (d) scanning both Δ and w with $\gamma_c = 1, I_s = 40, v = 3$, and $B = 4$.

pump intensity (I_s), with parameters $v = 3$, $w = 7$, $\gamma_c = 1$ and $B = 4$. The diagram highlights the critical thresholds at which the system transitions from stability to bistability and oscillatory behavior as I_s increases. For low input power levels, light propagates symmetrically in the CW and CCW directions through the nonlinear SSH lattice. However, when the input power reaches moderate levels ($I_s > 13$), spontaneous symmetry breaking occurs at specific detuning values, indicated by the green regions. This phenomenon reflects the sensitivity of the refractive index to input power. At higher input power levels, the system exhibits oscillatory behavior, represented by the yellow regions and bistability.

We have scanned detuning with the XPM strength B as shown in Fig. 5.2(b), for fixed parameters $I_s = 40$, $\gamma_c = 1$, $v = 3$, and $w = 7$. The diagram reveals the impact of increasing B on the emergence of stability, bistable, and oscillatory regimes. At low B values, the nonlinear SSH lattice exhibits two distinct phases: symmetric stability and oscillatory behavior. As the XPM strength increases, a bistability phase emerges. Notably, the bistability phase at specific detuning values corresponds to edge mode, whereas the oscillatory phases are associated with bulk modes. This highlights the interplay between nonlinear effects and the characteristics of the system.

Fig. 5.2(c) shows the phase diagram, scanning detuning, and coupling coefficient γ_c. We have set $I_s = 40$, $v = 3$, $w = 7$ and $B = 4$. The diagram highlights the gradual transitions between symmetric stability, bistability, and oscillatory behavior. When γ_c is set with small values, the system exhibits a single stable state, characterized by $I_{n,CW} = I_{n,CCW}$. However, once γ_c increases, both bistability and oscillatory regimes emerge. Oscillatory behavior corresponds to the excitation of bulk modes.

Since the coupling coefficients in the SSH lattice are important for observing edge modes, we have investigated the detuning range with the range of the inter-cell coupling coefficient w, as illustrated in Fig. 5.2(d). This analysis highlights the impact of variations in w on the system's dynamic, including symmetric stability, bistability, and oscillatory behavior, across the detuning range under the conditions $v = 3$, $I_s = 40$, and $B = 4$. A significant finding is that the bistability regime vanishes when $v = w$, marking the point at which the SSH lattice ceases to exhibit a trivial phase. However, this absence of bistability at $v = w$ is likely parameter-dependent; for other values of I_s or γ_c or v, bistability may still emerge.

To better understand this scenario, we have plotted Poincaré sections for weak and strong input intensities and compared it with a case of $v \neq w$ as illustrated in Figs. 5.3(a)- 5.3(c), respectively. Under weak input intensity, the CW and CCW modes propagate symmetrically, maintaining a stable state. However, at higher input intensities, the system exhibits stable, periodic, and chaotic oscillating. In the nonlinear SSH lattice with $v = w$, the periodic oscillations bistability regime is observed instead of the bistability regime for cases with $v \neq w$ as depicted in Figs. 5.3(b) and 5.3(c).

Furthermore, the light distribution loses its edge localization for specific detuning values. For example, when $\Delta = 1.18$ ($\Delta = 3.61$), the CCW (CW) mode becomes concentrated in the first three rings (the second ring), while the CW (CCW) mode remains localized at the left edge, as depicted in Fig. 5.4(a) and 5.4(b). Now to see the concentration of intensity in sublattices A and B, we have plotted the polarization in Fig. 5.4(d) for $v = w$ and compared it with a case of $v \neq w$, using Eq. (4.2). It is evident that the majority of the intensity, where polarization values approach unity, can be concentrated in sublattices A

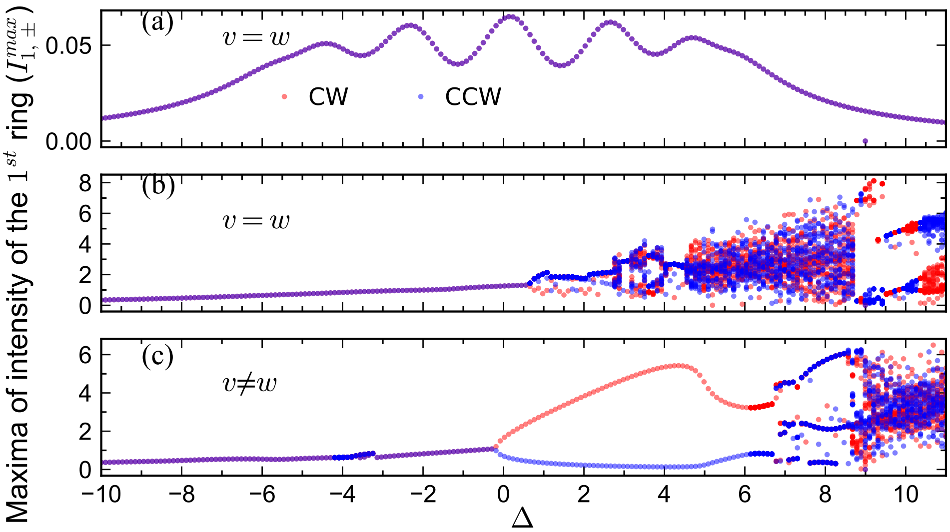

Figure 5.3: (a) The maxima of the CW and CCW intensity time series for the first ring resonator in a 1D SSH lattice consisting of seven ring resonators with $v = w = 3$, $A = 1$, $B = 4$ and $I_s = 1$ while $I_s = 40$ in (b). (c) For $v \neq w$ ($v = 3$, $w = 7$) with identical parameters that applied in b.

only when $v \neq w$. This intensity distribution constitutes a distinguishing feature of the topological edge mode. In contrast, the nonlinear SSH lattice with $v = w$ exhibits behavior analogous to the linear SSH lattice, implying that it does not support the emergence of a topological edge mode. To evaluate the intensity localization of dynamic modes across the entire SSH lattice, the participation ratio PR has been computed using Eq. (4.3) as illustrated in Fig. 5.4(e). We can clearly observe that for small detuning, $-10 \leq \Delta \leq -8$, the intensity is localized ($PR = 1$) for nonlinear SSH lattice with $v = w$ while is delocalized ($PR > 1$) with $v \neq w$. However, when detuning increases, intensity starts to concentrate at the edge of the system with $v \neq w$ while delocalizing in the case of $v = w$.

5.3 Dynamical mode decomposition

Until now, the analysis primarily focused on the evolutionary dynamics of the first ring without accounting for the spatial distribution when constructing phase

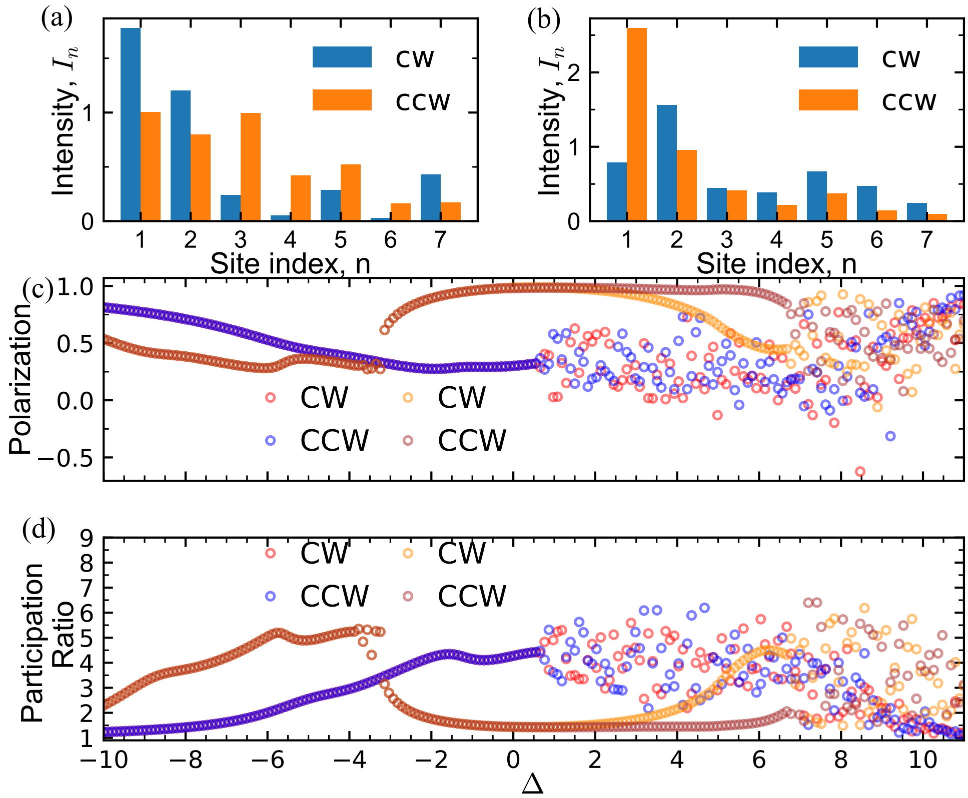

Figure 5.4: The intensity distribution in a 1D SSH lattice consisting of seven ring resonators with $v = w = 3$, $A = 1$, $B = 4$ and $I_s = 40$, for $\Delta = 1.18$ in (a) and $\Delta = 3.61$ in (b). (c) polarization in A and B sites. (d) Participation ratio for intensity. red and blue color for $v = w$, and brown and orange color for $v \neq w$ in (c&d).

diagrams or examining bistability and oscillatory phases. This limitation highlights the need for a more comprehensive approach that simultaneously captures both temporal variations and spatial distributions. By employing Dynamic Mode Decomposition (DMD), we can address this limitation and gain a clearer understanding of system dynamics. In this section, we will use the data we have collected from the results of the previous chapter. Before going through the details, we will start with a brief explanation of singular value decomposition, as it is an important stage in this analysis.

5.3.1 Singular value decomposition

The singular value decomposition (SVD) of a matrix $(m \times n)$ is the decomposition of X into the product of three matrices:

$$X = U\sigma V^{\dagger}, \tag{5.1}$$

where U is a matrix $(m \times m)$ of the orthonormal eigenvectors of $XX^{\dagger}$. $V^{\dagger}$ is the conjugate transpose of a $(n \times n)$ matrix has the orthonormal eigenvectors of $X^{\dagger}X$. σ is $(m \times n)$ rectangular diagonal matrix with positive real numbers on its diagonal; $\sigma_1 > \sigma_2 > \ldots > \sigma_{min(m,n)} \geq 0$ In the next section, we will perform SVD to reduce the size of the data matrix.

Dynamical mode decomposition (DMD) is a powerful tool for analyzing complex dynamical systems [96–99]. This method has been improved significantly since it was proposed in 2010 [97], as it has the capability to be applied to linear and nonlinear dynamics. It identifies the dominant spatial and temporal modes in a system's dynamics from data, which are important for understanding coherent structures in nonlinear phenomena such as oscillations. DMD works by extracting spatiotemporal structures from snapshot data $[x_1, x_2, x_3, x_4, \ldots, x_{Nt}]$

with zie $(N_s \times Nt)$ that are collected over time Nt for N_s sites. The dynamical mode decomposition method assumes that a sequence of snapshots captured from a dynamical system can be interconnected through a linear operator denoted as $\mathbf{A}$. This operator serves to relate each snapshot to the next, illustrating the evolution of the system over time. It is written as:

$$X_2 = \mathbf{A}X_1, \tag{5.2}$$

where X_1 and X_2 are data matrices with starting time step t_1 and t_2, respectively. Then, the data matrices can be given by:

$$X_1 = [x_1, x_2, x_3, x_4, \ldots, x_{Nt-1}], \tag{5.3}$$

and

$$X_2 = [x_2, x_3, x_4, x_5, \ldots, x_{Nt}]. \tag{5.4}$$

We apply SVD to capture the dominant patterns and discard less important components of X_1, then reduce computational complexity. It becomes:

$$X_1 = U_r \sigma_r V_r^\dagger. \tag{5.5}$$

By substituting in Eq. (5.2):

$$X_2 = \mathbf{A} U_r \sigma_r V_r^\dagger. \tag{5.6}$$

To reduce the linear operator $\mathbf{A}$, it is projected into the truncated proper orthogonal decomposition subspace:

$$\mathbf{A}_r = U_r^\dagger X_2 V_r \sigma_r^{-1}. \tag{5.7}$$

The eigenvalues Λ and eigenvectors W of the reduced linear operator $\mathbf{A}_r$:

$$\mathbf{A}_r W = W\Lambda. \tag{5.8}$$

Then, the DMD modes are given by:

$$\mathbf{\Phi} = X_2 V \sigma^{-1} W. \tag{5.9}$$

We will apply the DMD analysis on time series data that was used to plot the Poincaré section in Fig. 4.1 in the previous chapter. Here, consider $\Delta = 0.025$ and 4.02 corresponding to bistability, $\Delta = 7.3$ corresponding to periodic oscillations without switching, $\Delta = 7.51$ corresponding to periodic oscillations with switching, and $\Delta = 8.87$ corresponding to chaotic oscillations. Figures 5.5(a) and 5.5(c) show the normalization of singular values of the bistability regime with respect to the maximum one for small detuning values; $\Delta = 0.025$ and $\Delta = 4.02$. The nonlinear SSH lattice exhibits one mode for both cases, corresponding to the bistability phase. The field amplitude of the first DMD modes shows localization at one edge and decreases exponentially through the bulk as illustrated in Figs. 5.5(b) and Figs 5.5(d). However, the majority of field amplitude with $\Delta = 4.02$ is on the sublattice A (odd sites), showing the feature of edge mode.

For the periodic oscillation regime without switching between CW and CCW modes, we observed more modes and different distributions when analyzing time-set data at large detuning values. For instance, at $\Delta = 7.3$ as depicted in Figure 5.6(a), there are three DMD modes indicate that the optical intensity oscillates in CW and CCW direction through nonlinear SSH lattice. The corresponding field distributions, depicted in Figs. 5.6(b) - 5.6(d), demonstrate the absence of edge mode due to the excitation detuning being situated within the

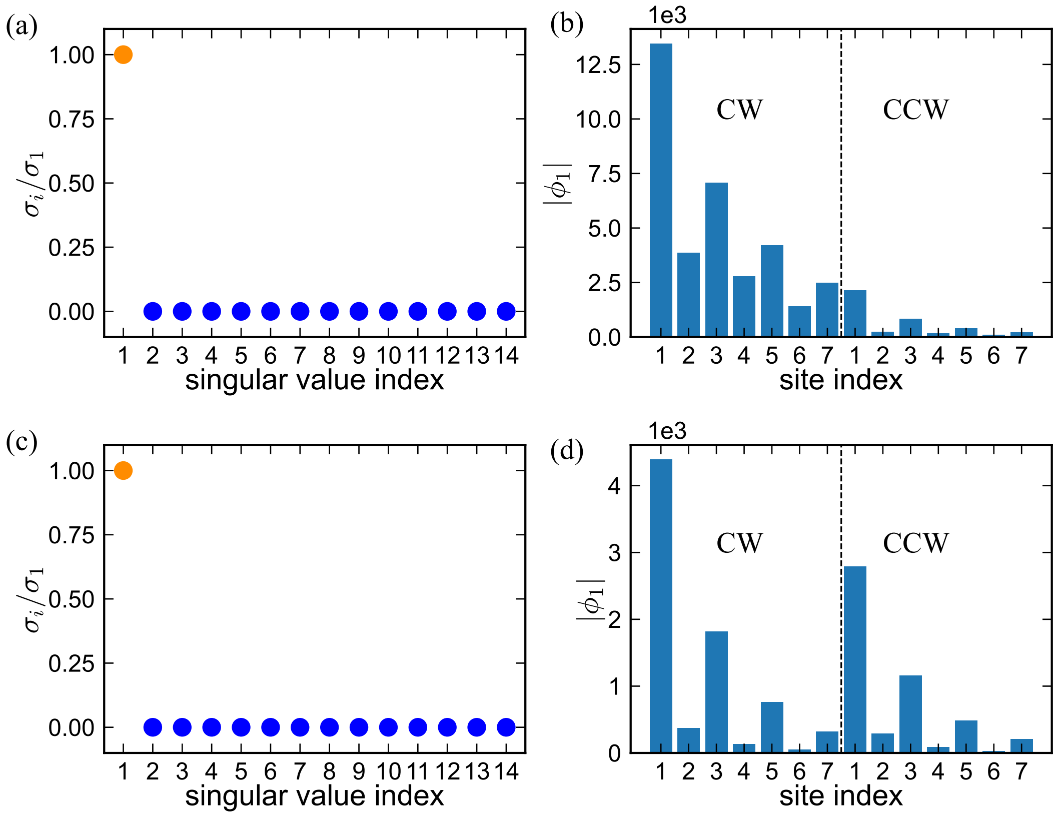

Figure 5.5: DMD analysis for bistability regime. (a) Singular values for $\Delta = 0.025$. (b) the field amplitude profile of the first singular value in a. (c) Singular values for $\Delta = 4.02$. (d) the field amplitude profile of the first singular value in c.

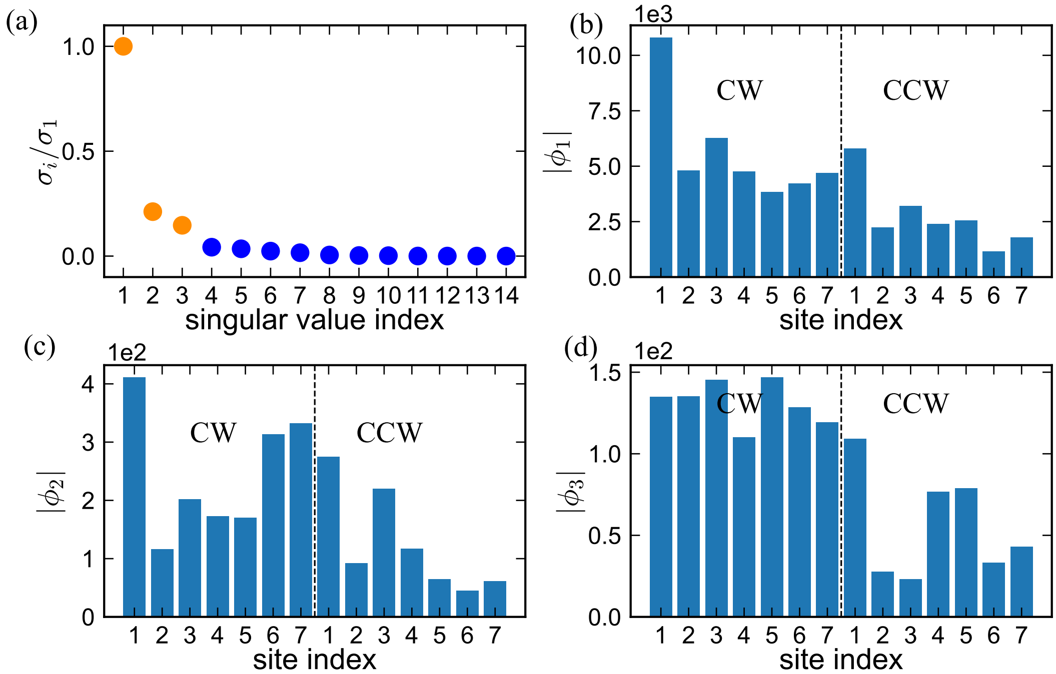

Figure 5.6: DMD analysis for a periodic regime with no switching with $\Delta = 7.3$. (a) Singular values. The field amplitude profile of the first, second and third singular value in (b), (c), (d), respectively

bulk region.

In contrast, periodic oscillations with switching between CW and CCW modes require more than three modes, as illustrated in Fig. 5.7(a). The field profiles corresponding to the first three modes, which characterize the bulk modes, are presented in Figs. 5.7(b)- 5.7(d).

Figure 5.8 shows the DMD results for the chaotic oscillating regime with $\Delta = 8.87$. The nonlinear SSH lattice has more DMD modes than in the periodic regimes. There are six DMD modes with $\sigma/\sigma_1 > 0.1$ in a periodic regime as shown in Fig. 5.7(a) while eight DMD modes with $\sigma/\sigma_1 > 0.1$ in a chaotic regime as shown in Fig. 5.8(a). The DMD modes for the chaotic oscillating regime exhibit finite amplitudes across both the A (odd sites) and B (even sites), similar to periodic oscillation regimes sublattices as depicted in Figs. 5.8(b)- 5.8(d).

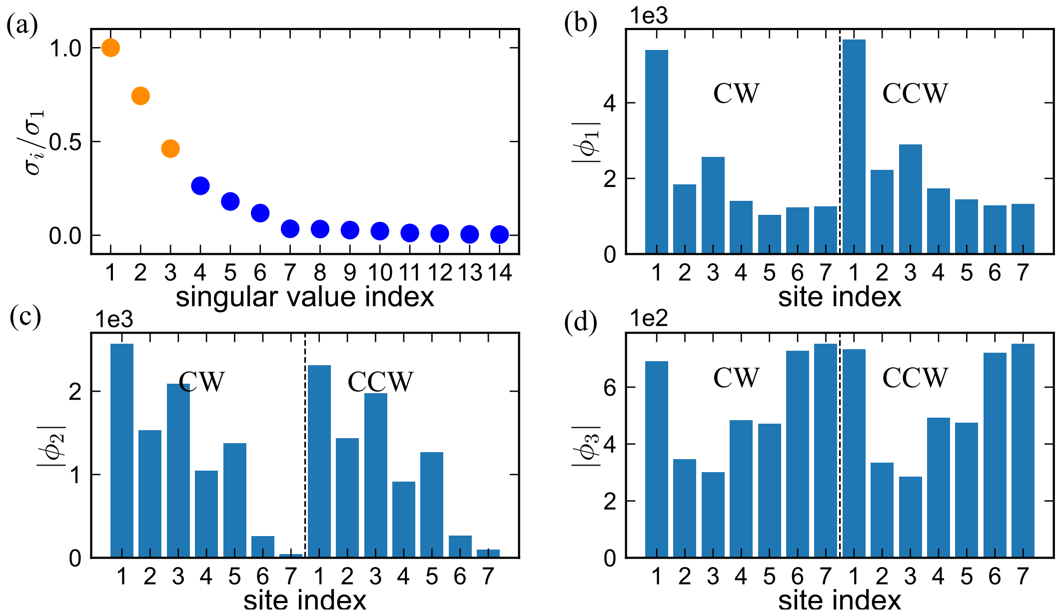

Figure 5.7: DMD analysis for a periodic regime with switching with $\Delta = 7.51$. (a) Singular values. The field amplitude profile of the first, second and third singular value in (b), (c), (d), respectively

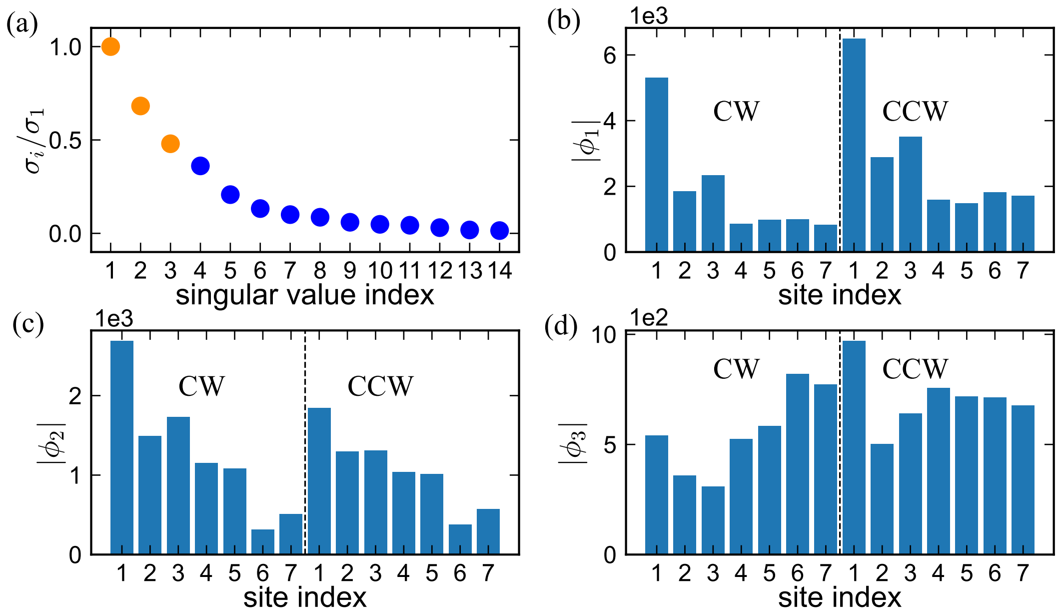

Figure 5.8: DMD analysis for a chaotic regime with no switching, with $\Delta = 8.87$. (a) Singular values. The field amplitude profile of the first, second and third singular value in (b), (c), (d), respectively

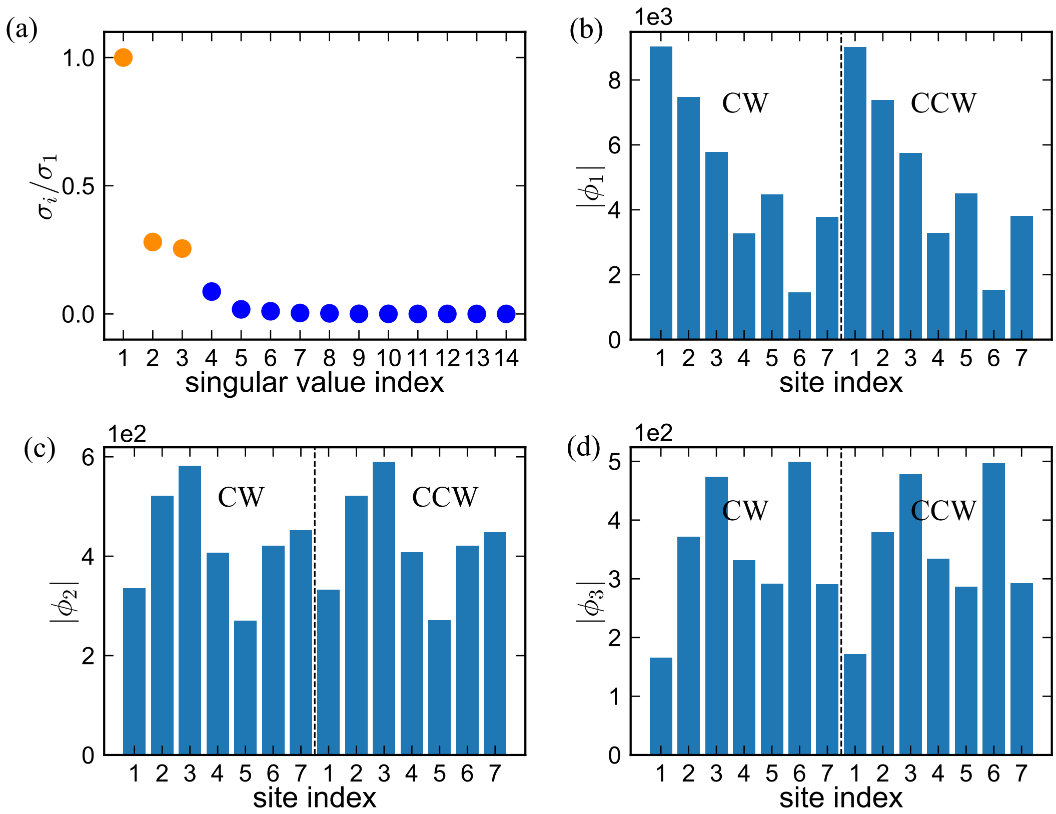

Figure 5.9: DMD analysis for the periodic regime in SSH lattice with detuning $\Delta = 1.18$ and $v = w = 3$. (a) Singular values. The field amplitude profile of the first three singular values is marked by an orange color in (b), (c), and (d), respectively.

Now, we will apply DMD analysis to the case of $v = w$ on time series data, which we have used in plotting phase diagram Fig. 5.4(b). Figure 5.9 shows the DMD results for a periodic oscillating regime with detuning $\Delta = 1.18$. Similar to the case of $v \neq w$ for periodic regimes, there is more than one mode. These modes feature the bulk mode, showing finite amplitude in each site as illustrated in Figs. 5.9(b)- 5.9(d) for modes marked by orange color. More modes can be observed for chaotic oscillation regimes, such as with detuning $\Delta = 3.61$ as shown in Fig 5.10(a) compared with periodic cases. However, the amplitudes distributed across sublattices A and B, as shown in Figs. 5.10(b)- 5.10(d), which are similar in periodic regimes.

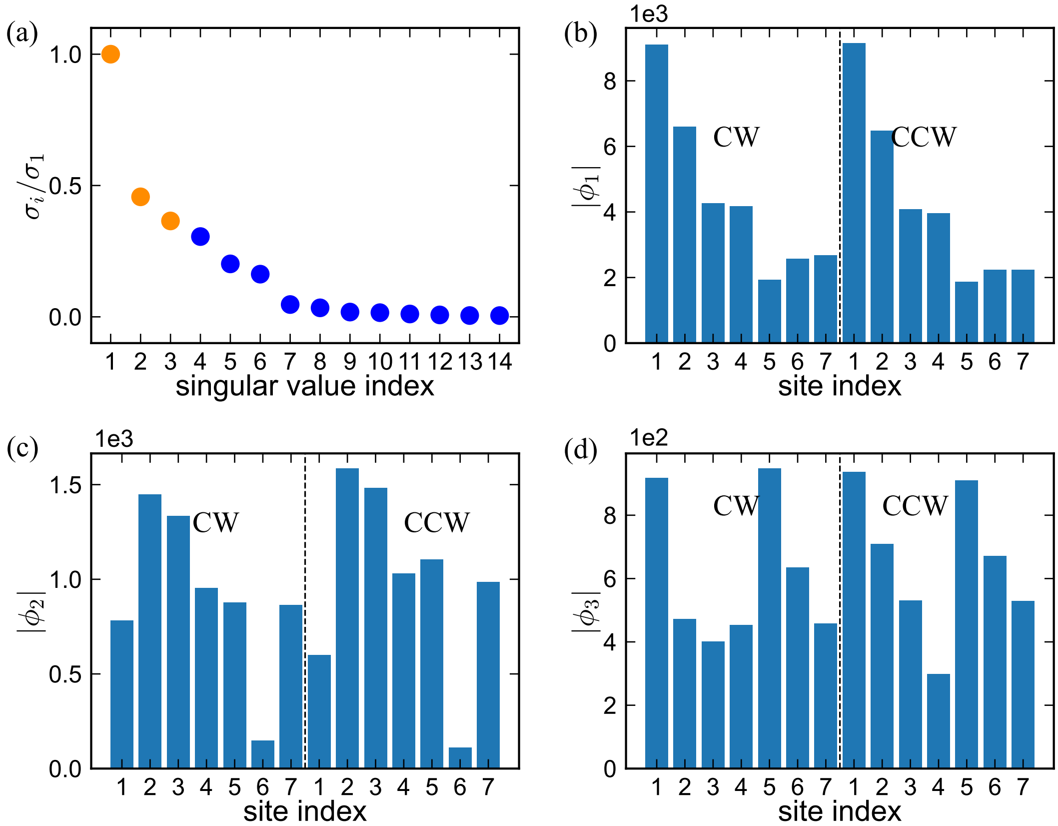

Figure 5.10: DMD analysis for the oscillations regime in SSH lattice with detuning $\Delta = 3.16$ and $v = w = 3$. (a) Singular values. The field amplitude profile of the first DMD mode (b), the second DMD mode (c), and (d) of the DMD mode.

5.4 Summary

In this chapter, we have looked at the phase diagram and dynamical mode decomposition as numerical tools to explore the behavior of the optical SSH system with Kerr nonlinearity. The phase diagram provides a comprehensive overview of the system's regimes depending on the dynamic of CW and CCW modes under varying input parameters, such as detuning and input power, highlighting transitions between distinct dynamic behaviors, including steady states, bistability, and oscillations. Also, we have compared the nonlinear SSH lattice with reciprocal and non-reciprocal coupling coefficients. DMD is employed to gain deeper insights into the underlying temporal and spatial dynamics of the system. Using singular value decomposition, DMD identifies dominant modes and their contributions to the overall dynamics. We have observed a single mode in the bistability regimes, whereas more than two modes in the oscillation regimes. The edge mode can be captured only in a bistability regime at a certain detuning value.

Chapter 6

Conclusions and future research directions

6.1 Conclusions

In this thesis, we have explored the nonlinear dynamics of topological photonic systems, focusing on optical bistability and oscillatory behaviors of CW and CCW modes in the 1D Su-Schrieffer-Heeger lattice with Kerr nonlinearity.

We have started in Chapter 3 by adapting the Lugiato-Lefever equation to model the field amplitudes in the SSH lattice composed of ring resonators with Kerr nonlinearity. It demonstrates the emergence of the optical bistability phase under varying pump intensities. Our results showed that the CW and CCW mode intensities in the first ring resonator remain symmetric up to a critical pump intensity, beyond which spontaneous symmetry breaking occurs due to the increasing refractive index and then splitting of resonance frequencies in the CW and CCW modes. It is followed by spontaneous symmetry breaking in the other rings.

In chapter 4, we have investigated a strong interaction between CW and

CCW modes via XPM at different input power. By using Poincaré sections, the maxima of intensity in CW and CCW modes have been mapped as a function of detuning at various input power levels. We have observed that the nonlinear SSH lattice exhibits remarkable optical bistability at higher input powers and oscillatory behaviors, including periodic and chaotic oscillations. Additionally, we have analyzed key features of the system, including the asymmetry between CW and CCW intensities, polarization characteristics at sublattice A and B sites, and the participation ratio for intensity distributions. These analyses provide valuable insights into the intricate interplay between edge and bulk modes and the overall dynamics of the nonlinear SSH lattice.

In chapter 5, we have presented a detailed investigation into the phase diagrams and dynamical DMD as powerful analytical tools for understanding the behavior of the optical SSH system with Kerr nonlinearity. The phase diagram serves as a crucial framework for characterizing the system's dynamic regimes, governed by the interplay of CW and CCW modes, under varying input parameters such as detuning and input power. These diagrams show transitions between distinct behaviors: steady states, optical bistability, and oscillatory dynamics. The optical bistability cannot be observed when $v = w$ under the specific parameters used in our analysis.

Additionally, we have employed DMD to analyze the temporal and spatial dynamics of the system, offering a deeper insight into its behavior. By employing singular value decomposition, DMD identifies the dominant modes contributing to the dynamics and facilitates the extraction of spatiotemporal structures. This analysis demonstrates edge and bulk modes depending on the time set data for all sites in nonlinear SSH lattice.

6.2 Future directions

This work has investigated the role of Kerr nonlinearity in shaping the dynamics of edge and bulk modes within the Su-Schrieffer-Heeger lattice. While significant progress has been made, several avenues for further investigation remain:

- Experimental implementation of the nonlinear SSH lattice using photonic platforms such as silicon microring resonators [78] to observe whether the predicted optical bistability and oscillatory phases can be consistently replicated in realistic systems.
- Investigation of type oscillations using Lyapunov exponent [100].
- Examination of the robustness of the edge mode and bistability in the presence of structural disorder or environmental perturbations.
- Investigation of the interplay of Kerr nonlinearity with non-Hermitian physics by considering gain saturation.
- Including group velocity dispersion (anomalous or normal) to restore the original partial differential equation form of the Lugiato-Lefever model [101]. This approach would enable a detailed studying of how resonator coupling influences soliton dynamics, which play a key role in the frequency combs generation.

Appendix

Appendix A

Derivation of the Lugiato-Lefever equation

We derive the spatial Lugiato–Lefever equation, which governs the dynamics of an optical field inside a cavity, starting from the fundamental Nonlinear Schrödinger equation (NLSE) and incorporating the effects of cavity boundary conditions under the mean-field approximation. This derivation is based on the work by G.-L. Oppo and W.J. Firth [101].

The propagation of a coherent optical field $E(x, y, z, t)$ within a Kerr medium is described by the NLSE:

$$\frac{\partial E}{\partial z} + \frac{n}{c}\frac{\partial E}{\partial t} = i\frac{1}{2k}\nabla^2 E + i\eta|E|^2 E, \tag{A.1}$$

where z denotes the longitudinal propagation coordinate, t is time, n is the linear refractive index of the medium, c is the speed of light in vacuum, k is the wavevector, $\nabla^2 = \frac{\partial^2}{\partial x^2} + \frac{\partial^2}{\partial y^2}$ is the transverse Laplacian, and η represents the self-focusing ($\eta = +1$) and self-defocusing ($\eta = -1$) media.

The cavity imposes boundary conditions on the field at the entrance of the

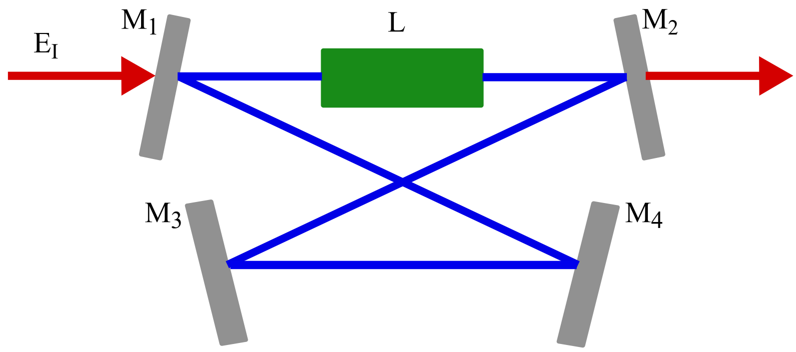

Figure A.1: The bow-tie cavity with four mirrors (M), E_I is input field and L is the length of the nonlinear medium

nonlinear medium ($z = 0$):

$$E(x, y, 0, t) = e^D E\left(x, y, L, t - \frac{\Lambda - L}{c}\right) + \sqrt{T} E_I(x, y), \tag{A.2}$$

where L is the length of the nonlinear medium, Λ is the total cavity length, T is the field transmission coefficient of the input mirror, $R = 1 - T$ is the reflectivity, and E_I is the input field. The complex operator D encapsulates cavity losses, detuning, and diffraction:

$$D = \ln\sqrt{R} - i\Theta + (\Lambda - L)\frac{i}{2k}\nabla^2,$$

with the detuning parameter $\Theta = \frac{\omega_c - \omega}{c}\Lambda$, where ω and ω_c are the frequencies of the input field and the nearest cavity resonance, respectively.

Assuming that the cavity mirrors are highly reflective, i.e., $T \ll 1$ (small losses), and that field variations over a single round trip are small, the boundary condition can be simplified. To incorporate the boundary condition Eq. A.2 into the propagation equation Eq. A.1, standard mean field limit (MFL) approximation is applied:

$$z' = z, \qquad t' = t + \left[\frac{\Lambda - L}{c}\right] \cdot \frac{z}{L}. \tag{A.3}$$

Based on the condition A.2, LHS of Eq. A.1 becomes:

$$\frac{\partial E}{\partial z} + \frac{n}{c}\frac{\partial E}{\partial t} = \frac{\partial E}{\partial z'} + \left(\frac{\Lambda - L}{cL}\right)\frac{\partial E}{\partial t'} + \frac{n}{c}\frac{\partial E}{\partial t'}. \tag{A.4}$$

$$\frac{\partial E}{\partial z} + \frac{n}{c}\frac{\partial E}{\partial t} = \left(\frac{\partial}{\partial z'} + \frac{\Lambda + (n-1)L}{cL}\frac{\partial}{\partial t'}\right)E. \tag{A.5}$$

Defining a new field variable F, we obtain

$$F = \Gamma E + \sqrt{T}E_I\frac{z}{L}, \quad \text{where } \Gamma = e^{D\frac{z}{L}}.$$

Then, we invert this:

$$E = \Gamma^{-1}\left(F - \sqrt{T}E_I(z = L)\right).$$

Now, we plug into the transformed NLSE:

$$\frac{\partial F}{\partial t'} + \frac{cL}{\Lambda + (n-1)L}\frac{\partial F}{\partial z'} = \\ \frac{c}{\Lambda + (n-1)L}\left[\frac{D}{L}\left(F - TE_I\frac{z}{L}\right) + \Gamma\left(i\frac{1}{2k}\nabla^2 E + i\eta|E|^2E\right) + \sqrt{T}E_I\frac{1}{L}\right]. \tag{A.6}$$

The boundary conditions Eq. A.2 are transformed into

$$F(x, y, 0, t') = F(x, y, L, t'). \tag{A.7}$$

Within the MFL framework, assuming that both detuning Θ and $1/(2k)$ are $\mathcal{O}(\epsilon) \ll 1$, one can get that:

$$D \approx -\frac{T}{2} - i\Theta + i\frac{\Lambda - L}{2k}\nabla^2, \quad \Gamma \approx 1 + \frac{D}{L}z. \tag{A.8}$$

By plugging Eq. A.8 in Eq. A.6 and at the first order in ϵ is given

$$
\begin{aligned}
\frac{\partial F}{\partial t'} + \frac{cL}{\Lambda + (n-1)L}\frac{\partial F}{\partial z'} = \\
-\frac{cT/2}{\Lambda + (n-1)L}F - i\frac{c\Theta}{\Lambda + (n-1)L}F + i\frac{c\,(\Lambda - L)}{2k\,[\Lambda + L\,(n-1)]}\nabla^2 F \\
+ \frac{c\sqrt{T}}{\Lambda + L\,(n-1)}E_I + \frac{cL}{\Lambda + L\,(n-1)}i\eta|E|^2 E.
\end{aligned}
\tag{A.9}
$$

The evolution equation simplifies to

$$
\tau\frac{\partial F}{\partial t'} + L\frac{\partial F}{\partial z'} = -\frac{T}{2}F - i\Theta F + id\nabla^2 F + iL\eta|F|^2 F + \sqrt{T}E_I, \tag{A.10}
$$

where

$$
\tau = \frac{\Lambda + (n-1)L}{c}, \quad d = \frac{\Lambda - L}{2k}.
$$

Due to the synchronous and periodic nature of the revised longitudinal boundary condition (A.7), a Fourier expansion in longitudinal modes becomes applicable. Nonetheless, under the standard mean field limit approximation, only the mode nearest to ω possesses non-zero components. This mode is associated with a zero longitudinal frequency, leading to the condition $\frac{\partial F}{\partial z'} = 0$. Additionally, since Γ at zeroth order is equal to one, it follows that $F \approx E$. By dividing the equation by $T/2$, considering $L = \mathcal{O}(T/2)$, and introducing the renormalized parameters, one can obtain

$$
\frac{\partial E}{\partial(\kappa t')} = E_I - (1 + i\Delta)E + i\eta|E|^2 E + ia\nabla^2 E, \tag{A.11}
$$

where

$$
\Delta = \frac{\Theta}{T/2}, \quad a = \frac{(\Lambda - L)}{kT}, \quad \kappa = \frac{T}{2\tau}.
$$

This is the spatial Lugiato–Lefever equation, which describes the balance among input driving, cavity losses, Kerr nonlinearity, and transverse diffraction that underpins the formation of stationary patterns and localized cavity solitons within the system.

An analogous approach can be employed to obtain temporal Lugiato–Lefever equation for ring cavities. We consider group velocity dispersion term $\gamma \frac{\partial^2 E}{\partial t^2}$ instead of the term $\frac{1}{2k}\nabla^2$ in NLSE A.1, where γ is positive (negative) in the anomalous (normal) dispersion regime. Assuming a single transverse mode, but a large number of longitudinal cavity modes, one can obtain the temporal Lugiato–Lefever equation

$$\frac{\partial E}{\partial \bar{\kappa t'}} = E_{in} - E - i\Delta E + i\eta |E_|^2 E + i\beta \frac{\partial^2 E}{\partial \tau^2}, \tag{A.12}$$

where β is the group-velocity dispersion coefficient.

Appendix B

Sublattice symmetry and CW-CCW symmetry in SSH lattice

The linear SSH model(Fig. 3.1(b)), where $I_s \approx 0$, exhibits two distinctive symmetries: sublattice symmetry and CW-CCW symmetry. Although both are referred to as chiral symmetry in the literature, we use the terms sublattice symmetry and CW-CCW symmetry here for clarity. One can write the Hamiltonian of the SSH model using block matrix form as following :

$$\mathbf{H} = \begin{pmatrix} \mathbf{H}_{cw} & \mathbf{0} \\ \mathbf{0} & \mathbf{H}_{ccw} \end{pmatrix}, \tag{B.1}$$

where $\mathbf{H}_{cw}$ ($\mathbf{H}_{ccw}$) is $(M \times M)$ SSH Hamiltonian matrices for CW (CCW) modes. They can be expressed, respectively, as:

$$\mathbf{H}_{cw} = \begin{pmatrix} \mu_{1,a}^{cw} & v & 0 & 0 & \dots \\ v & \mu_{1,b}^{cw} & w & 0 & \dots \\ 0 & w & \ddots & \ddots & \vdots \\ \vdots & \vdots & \ddots & \ddots & \ddots \end{pmatrix}, \tag{B.2}$$

and

$$\mathbf{H}_{ccw} = \begin{pmatrix} \mu_{1,a}^{ccw} & v & 0 & 0 & \dots \\ v & \mu_{1,b}^{ccw} & w & 0 & \dots \\ 0 & w & \ddots & \ddots & \vdots \\ \vdots & \vdots & \ddots & \ddots & \ddots \end{pmatrix}. \tag{B.3}$$

The diagonal terms in Eq B.2 and Eq B.3, representing the onsite energy in a tight-binding description, accounting for the shift in resonance frequencies in sublattices; A ($\mu_{n,a}$) and B ($\mu_{n,b}$):

$$\mu_{n,a}^{cw} = -\Delta + |E_{an,+}|^2 + 2|E_{an,-}|^2, \tag{B.4}$$

and

$$\mu_{n,a}^{ccw} = -\Delta + |E_{an,-}|^2 + 2|E_{an,+}|^2. \tag{B.5}$$

$\mu_{n,b}^{cw}$ and $\mu_{n,b}^{ccw}$ are defined in a similar way.

Let us begin by examining the sublattice symmetry of the nonlinear SSH Hamiltonian. We define the sublattice symmetry operator $\mathbf{\Gamma}$, of size $2M \times 2M$, as:

$$\mathbf{\Gamma} = \begin{pmatrix} \mathbf{\Gamma}_M & \mathbf{0} \\ \mathbf{0} & \mathbf{\Gamma}_M \end{pmatrix}, \tag{B.6}$$

where $\mathbf{\Gamma}_M$ represents the subspace of size $M \times M$, given by:

$$\mathbf{\Gamma}_M = \begin{pmatrix} -1 & 0 & 0 & \dots \\ 0 & 1 & 0 & \dots \\ 0 & 0 & -1 & \ddots \\ \vdots & \vdots & \ddots & \ddots \end{pmatrix}. \tag{B.7}$$

By applying $\mathbf{\Gamma}$ to $\mathbf{H}_{cw}$ ($\mathbf{H}_{ccw}$), we obtain:

$$\mathbf{\Gamma}_M \mathbf{H}_{cw} \mathbf{\Gamma}_M^{\dagger} = \begin{pmatrix} \mu_{1,a}^{cw} & -v & 0 & 0 & \dots \\ -v & \mu_{1,b}^{cw} & -w & 0 & \dots \\ 0 & -w & \ddots & \ddots & \vdots \\ \vdots & \vdots & \ddots & \ddots & \ddots \end{pmatrix}, \tag{B.8}$$

and

$$\mathbf{\Gamma}_M \mathbf{H}_{ccw} \mathbf{\Gamma}_M^{\dagger} = \begin{pmatrix} \mu_{1,a}^{ccw} & -v & 0 & 0 & \dots \\ -v & \mu_{1,b}^{ccw} & -w & 0 & \dots \\ 0 & -w & \ddots & \ddots & \vdots \\ \vdots & \vdots & \ddots & \ddots & \ddots \end{pmatrix}. \tag{B.9}$$

This implies that the sublattice symmetry in the strong nonlinear regime is broken, as the diagonal terms of $\mathbf{H}_{cw}$ and $\mathbf{H}_{ccw}$ do not vanish, resulting in $\mathbf{\Gamma H \Gamma}^{\dagger} \neq -\mathbf{H}$. In contrast, with weak nonlinearity, the diagonal terms are approximately zero, resulting in $\mathbf{\Gamma H \Gamma}^{\dagger} = -\mathbf{H}$ and restoring the sublattice symmetry. For this analysis, we assume zero detuning.

Next, we investigate the CW-CCW symmetry by defining a block mirror symmetry operator matrix $\mathbf{P}$ as follows:

$$\mathbf{P} = \begin{pmatrix} \mathbf{0} & \mathbb{I}_M \\ \mathbb{I}_M & \mathbf{0} \end{pmatrix}. \tag{B.10}$$

Here, $\mathbb{I}_M$ represents an identity matrix of size $M \times M$. We then apply $\mathbf{P}$ to the full Hamiltonian as follows:

$$\mathbf{P}\mathbf{H}\mathbf{P}^{-1} = \begin{pmatrix} \mathbf{H}_{ccw} & \mathbf{0} \\ \mathbf{0} & \mathbf{H}_{cw} \end{pmatrix}. \tag{B.11}$$

From equations B.2, B.3, it can be seen that $\mathbf{P}\mathbf{H}\mathbf{P}^{-1} = \mathbf{H}$ holds only when $E_{n,-} = E_{n,+}$, which accounts for symmetric dynamic modes in the weak nonlinear regime. In the strong nonlinear regime, we obtain $\mathbf{P}\mathbf{H}\mathbf{P}^{-1} \neq \mathbf{H}$, resulting in asymmetrical dynamics.

Appendix C

Optical ring resonator

An optical ring resonator allows the light to circulate independently in opposite directions and gives rise an resonant effect for the light waves. The configuration of the optical ring resonator is composed of a closed loop of a waveguide and coupled to the linear waveguides. The incident light passes through the linear waveguide and is partially combined with the ring resonator in the coupling region as illustrated in Fig. C.1.

When the optical path length of a ring resonator equals multiple of the wavelength, the ring resonator starts to be in resonance, i.e. the light propagating along the waveguide and the light propagating in the ring resonator interfere constructively. Then, the optical power in the ring resonator increases because the energies are accumulated at resonance. The condition of resonance can be written as:

$$m\lambda_{res} = n_{eff}L, \tag{C.1}$$

where m is an integer number that indicates the mode number, λ_{res} is the resonance wavelength, n_{eff} is the effective refractive index and L is the circumference of the ring resonator. The distance between two resonance frequencies is called

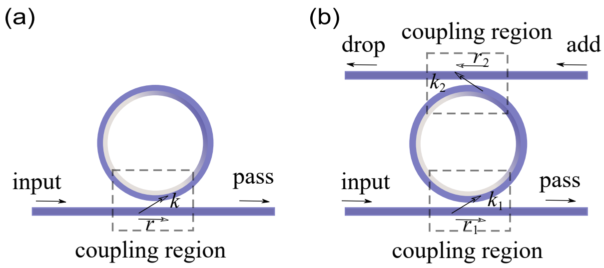

Figure C.1: (a) all-pass and (b) add-drop optical ring resonators configurations

the free spectral range, $FSR = \lambda_{res}^2/n_g L$, n_g refers to the group index in the denominator. The narrowness of resonances relative to their frequency is called finesse, $Finesse = FSR/FWHM$.

The simplest structure of the optical ring resonator contains one linear waveguide along with a ring resonator as illustrated in Fig. C.1 (a). This is known as an all-pass filter (APF) [78]) because at the resonant wavelength, the light coupled back from the ring interferes destructively with the light in the linear waveguide, canceling it out. As a result, no light is transmitted forward at that wavelength, effectively filtering out that specific wavelength. The input light goes through the waveguide and some portion of this light splits into a ring resonator with coupling k. following light propagation around the ring resonator, some light combines back to the linear waveguide and interferes with the incident light. The ratio of the transmitted and input field is written as [102]

$$\frac{E_{pass}}{E_{input}} = \exp i(\pi + \phi)\frac{a - r\exp(i\phi)}{1 - ra\exp(-i\phi)}, \tag{C.2}$$

where $\phi = \beta L$ is the round-trip phase shift with propagating constant β, a is the ring resonator loss coefficient and r is self-coupling.

The power transmission to the pass port T_{APF} can be determined from Eq.C.2

$$T_{APF} = \frac{|E_{pass}|^2}{|E_{input}|^2} = \frac{a^2 - 2ra\cos\phi + r^2}{1 - 2ra\cos\phi + (ra)^2}, \tag{C.3}$$

The power splitting ratios satisfy that $r^2+k^2=1$ as long as there are no losses in the coupling region. When the loss coefficient is equivalent to self-coupling, there is no power transmitted through the ring resonator. This is known as critical coupling. The phase shift of the transmitted light is derived by the argument as

$$\begin{aligned}\Phi &= \tan\left(\frac{E_{pass}}{E_{input}}\right), &\text{(C.4)}\\ &= \pi+\phi+\tan^{-1}\left(\frac{rsin\phi}{a-r\cos\phi}\right)+\tan^{-1}\left(\frac{ra\sin\phi}{1-ra\cos\phi}\right). &\text{(C.5)}\end{aligned}$$

The second configuration of the optical ring resonator in Fig. C.1 consists of a ring resonator coupled with two straight waveguides, there are four ports: input, pass, add and drop ports. The power transmission to the pass (T_p) and drop (T_d) port are given by

$$T_p = \frac{r_2^2a^2-2r_1r_2a\cos\phi+r_1^2}{1-2r_1r_2a\cos\phi+(r_1r_2a)^2}, \tag{C.6}$$

$$T_d = \frac{(1-r_1^2)(1-r_2^2)a^2}{1-2r_1r_2a\cos\phi+(r_1r_2a)^2}, \tag{C.7}$$

where the subscript number 1 and 2 indicate upper and lower coupling regions, respectively in Fig. C.1(b) [78]. In case of symmetric cross-coupling ($k_1 = k_2$) that induces critical coupling.

Bibliography

1. Klitzing, K. V., Dorda, G. & Pepper, M. New method for high-accuracy determination of the fine-structure constant based on quantized Hall resistance. *Physical Review Letters* **45,** 494–497 (1980).
2. Wang, Z., Chong, Y., Joannopoulos, J. D. & Soljačić, M. Observation of unidirectional backscattering-immune topological electromagnetic states. *Nature* **461,** 772–775 (2009).
3. Hafezi, M., Mittal, S., Fan, J., Migdall, A. & Taylor, J. M. Imaging topological edge states in silicon photonics. *Nature Photonics* **7,** 1001–1005 (2013).
4. Ozawa, T., Price, H. M., Amo, A., Goldman, N., Hafezi, M., Lu, L., Rechtsman, M. C., Schuster, D., Simon, J., Zilberberg, O. & Carusotto, I. Topological photonics. *Reviews of Modern Physics* **91,** 015006 (2019).
5. Lu, L., Joannopoulos, J. D. & Soljačić, M. Topological photonics. *Nature Photonics* **8,** 821–829 (2014).
6. Lu, L., Joannopoulos, J. D. & Soljačić, M. Topological states in photonic systems. *Nature Physics* **12,** 626–629 (2016).
7. Khanikaev, A. B. & Shvets, G. Two-dimensional topological photonics. *Nature Photonics* **11,** 763–773 (2017).

8. Xie, B.-Y., Wang, H.-F., Zhu, X.-Y., Lu, M.-H., Wang, Z. D. & Chen, Y.-F. Photonics meets topology. *Optics Express* **26,** 24531–24550 (2018).

9. Sun, X.-c., He, C., Liu, X.-p., Lu, M.-h. & Zhu, S.-n. Progress in quantum electronics two-dimensional topological photonic systems. *Progress in Quantum Electronics* **55,** 52–73 (2017).

10. Rider, M. S., Palmer, S. J., Pocock, S. R., Xiao, X., Arroyo Huidobro, P. & Giannini, V. A perspective on topological nanophotonics: current status and future challenges. *Journal of Applied Physics* **125,** 120901 (2019).

11. Maczewsky, L. J., Heinrich, M., Kremer, M., Ivanov, S. K., Ehrhardt, M., Martinez, F., Kartashov, Y. V., Konotop, V. V., Torner, L., Bauer, D. & Szameit, A. Nonlinearity-induced photonic topological insulator. *Science* **370,** 701–704 (2020).

12. Efremidis, N. K. Topological photonic Su-Schrieffer-Heeger-type coupler. *Physical Review A* **104,** 053531 (2021).

13. Arkhipova, A. A., Ivanov, S. K., Zhuravitskii, S. A., Skryabin, N. N., Dyakonov, I. V., Kalinkin, A. A., Kulik, S. P., Kompanets, V. O., Chekalin, S. V., Kartashov, Y. V. & Zadkov, V. N. Observation of nonlinearity-controlled switching of topological edge states. *Nanophotonics. Nanophotonics* **11,** 3653–3661 (2022).

14. Sohn, B.-U., Huang, Y.-X., Choi, J. W., Chen, G. F. R., Ng, D. K. T., Yang, S. A. & Tan, D. T. H. A topological nonlinear parametric amplifier. *Nature Communications* **13,** 7218 (2022).

15. Ivanov, S. K., Kartashov, Y. V. & Torner, L. Light bullets in Su-Schrieffer-Heeger photonic topological insulators. *Physical Review A* **107,** 033514 (2023).

16. Cáceres-Aravena, G., Real, B., Guzmán-Silva, D., Vildoso, P., Salinas, I., Amo, A., Ozawa, T. & Vicencio, R. A. Edge-to-edge topological spectral transfer in diamond photonic lattices. *APL Photonics* **8,** 80801 (2023).

17. Kartashov, Y. V. & Konotop, V. V. Topological star junctions: linear modes and solitons. *Chaos, Solitons Fractals* **179,** 114461 (2024).

18. Pérez, G. O., Dueñas, J. M., Guzmán-Silva, D., Torres, L. E. F. F. & Hermann-Avigliano, C. Transport of non-classical light mediated by topological domain walls in a SSH photonic lattice. *Scientific Reports* **14,** 12435 (2024).

19. Liu, X., Lin, Z., Song, W., Sun, J., Huang, C., Wu, S., Xiao, X., Xin, H., Zhu, S. & Li, T. Perfect excitation of topological states by supersymmetric waveguides. *Physical Review Letters* **132,** 016601 (2024).

20. Zhou, C., Xie, Z., Lei, T., Zhang, Y., Chen, Q. & Yuan, X. Optical mode-controlled topological edge state in waveguide lattice. *Nanophotonics. Nanophotonics* **13,** 319–325 (2024).

21. Sabour, K. & Kartashov, Y. V. Topological solitons in coupled Su–Schrieffer–Heeger waveguide arrays. *Optics Letters* **49,** 3580–3583 (2024).

22. Jörg, C., Jürgensen, M., Mukherjee, S. & Rechtsman, M. C. Optical control of topological end states via soliton formation in a 1D lattice. *Nanophotonics. Nanophotonics* **14,** 769–775 (2025).

23. Slobozhanyuk, A. P., Poddubny, A. N., Miroshnichenko, A. E., Belov, P. A. & Kivshar, Y. S. Subwavelength topological edge states in optically resonant dielectric structures. *Physical Review Letters* **114,** 123901 (2015).

24. Kartashov, Y. V. & Skryabin, D. V. Bistable topological insulator with exciton-polaritons. *Physical Review Letters* **119,** 253904 (2017).

25. Saei Ghareh Naz, E., Fulga, I. C., Ma, L., Schmidt, O. G. & van den Brink, J. Topological phase transition in a stretchable photonic crystal. *Physical Review A* **98,** 033830 (2018).

26. Zhang, W., Chen, X., Kartashov, Y. V., Skryabin, D. V. & Ye, F. Finite-dimensional bistable topological insulators: from small to large. *Laser Photonics Reviews* **13,** 1–7 (2019).

27. D'Aguanno, G., Hadad, Y., Smirnova, D. A., Ni, X., Khanikaev, A. B. & Alù, A. Nonlinear topological transitions over a metasurface. *Physical Review B* **100,** 214310 (2019).

28. Wei, M.-S., Liao, M.-J., Wang, C., Zhu, C., Xu, J. & Yang, Y. Phase transition and dynamics of qubits in coupled-cavity arrays with nonlinear topological photonics. *Results in Physics* **45,** 106232 (2023).

29. Parto, M., Wittek, S., Hodaei, H., Harari, G., Bandres, M. A., Ren, J., Rechtsman, M. C., Segev, M., Christodoulides, D. N. & Khajavikhan, M. Edge-mode lasing in 1D topological active arrays. *Physical Review Letters* **120,** 113901 (2018).

30. Poddubny, A., Miroshnichenko, A., Slobozhanyuk, A. & Kivshar, Y. Topological Majorana states in zigzag chains of plasmonic nanoparticles. *ACS Photonics* **1,** 101–105 (2014).

31. Sinev, I. S., Mukhin, I. S., Slobozhanyuk, A. P., Poddubny, A. N., Miroshnichenko, A. E., Samusev, A. K. & Kivshar, Y. S. Mapping plasmonic topological states at the nanoscale. *Nanoscale* **7,** 11904–11908 (2015).

32. Ling, C. W., Xiao, M., Chan, C. T., Yu, S. F. & Fung, K. H. Topological edge plasmon modes between diatomic chains of plasmonic nanoparticles. *Optics Express* **23,** 2021 (2015).

33. Rechtsman, M. C., Zeuner, J. M., Plotnik, Y., Lumer, Y., Podolsky, D., Dreisow, F., Nolte, S., Segev, M. & Szameit, A. Photonic Floquet topological insulators. *Nature* **496,** 196–200 (2013).

34. Verbin, M., Zilberberg, O., Kraus, Y. E., Lahini, Y. & Silberberg, Y. Observation of topological phase transitions in photonic quasicrystals. *Physical Review Letters* **110,** 76403 (2013).

35. Bahari, B., Ndao, A., Vallini, F., El Amili, A., Fainman, Y. & Kanté, B. Nonreciprocal lasing in topological cavities of arbitrary geometries. *Science* **358,** 636–640 (2017).

36. Slobozhanyuk, A., Mousavi, S. H., Ni, X., Smirnova, D., Kivshar, Y. S. & Khanikaev, A. B. Three-dimensional all-dielectric photonic topological insulator. *Nature Photonics* **11,** 130–136 (2017).

37. Haldane, F. D. M. & Raghu, S. Possible realization of directional optical waveguides in photonic crystals with broken time-reversal symmetry. *Physical Review Letters* **100,** 013904 (2008).

38. Raghu, S. & Haldane, F. D. M. Analogs of quantum-Hall-effect edge states in photonic crystals. *Physical Review A* **78,** 033834 (2008).

39. Smirnova, D., Leykam, D., Chong, Y. & Kivshar, Y. Nonlinear topological photonics. *Applied Physics Reviews* **7,** 021306 (2020).

40. Jalali Mehrabad, M., Mittal, S. & Hafezi, M. Topological photonics: fundamental concepts, recent developments, and future directions. *Physical Review A* **108,** 040101 (2023).

41. Dobrykh, D. A., Yulin, A. V., Slobozhanyuk, A. P., Poddubny, A. N. & Kivshar, Y. S. Nonlinear control of electromagnetic topological edge states. *Physical Review Letters* **121,** 163901 (2018).

42. Roy, A., Parto, M., Nehra, R., Leefmans, C. & Marandi, A. Topological optical parametric oscillation. *Nanophotonics* **11,** 1611–1618 (2022).

43. Xia, S., Kaltsas, D., Song, D., Komis, I., Xu, J., Szameit, A., Buljan, H., Makris, K. G. & Chen, Z. Nonlinear tuning of PT symmetry and non-Hermitian topological states. *Science* **372,** 72–76 (2021).

44. Sone, K., Ezawa, M., Gong, Z., Sawada, T., Yoshioka, N. & Sagawa, T. Transition from topological to chaos in the nonlinear Su-Schrieffer-Heeger model. *arXiv:2403.03038v2,* 1–17 (2024).

45. Li, X., Rui, G., He, J. & Gu, B. Nonlinear control of topological corner and edge states in a loop resonator. *Optics Communications* **550,** 130004 (2024).

46. Szameit, A. & Rechtsman, M. C. Discrete nonlinear topological photonics. *Nature Physics* **20,** 905–912 (2024).

47. Hadad, Y., Khanikaev, A. B. & Alù, A. Self-induced topological transitions and edge states supported by nonlinear staggered potentials. *Physical Review B* **93,** 155112 (2016).

48. Hadad, Y., Vitelli, V. & Alu, A. Solitons and propagating domain walls in topological resonator arrays. *ACS Photonics* **4,** 1974–1979 (2017).

49. Chaunsali, R. & Theocharis, G. Self-induced topological transition in phononic crystals by nonlinearity management. *Physical Review B* **100,** 014302 (2019).

50. Guo, M., Xia, S., Wang, N., Song, D., Chen, Z. & Yang, J. Weakly nonlinear topological gap solitons in Su–Schrieffer–Heeger photonic lattices. *Optics Letters* **45,** 6466 (2020).

51. Xia, S., Jukić, D., Wang, N., Smirnova, D., Smirnov, L., Tang, L., Song, D., Szameit, A., Leykam, D., Xu, J., Chen, Z. & Buljan, H. Nontrivial coupling of light into a defect: the interplay of nonlinearity and topology. *Light: Science Applications* **9,** 147 (2020).

52. Ma, Y.-P. & Susanto, H. Topological edge solitons and their stability in a nonlinear Su-Schrieffer-Heeger model. *Physical Review E* **104,** 054206 (2021).

53. Johansson, M. Topological edge breathers in a nonlinear Su-Schrieffer-Heeger lattice. *Physics Letters A* **458,** 128593 (2023).

54. Bai, K., Li, J.-Z., Liu, T.-R., Fang, L., Wan, D. & Xiao, M. Arbitrarily configurable nonlinear topological modes. *Physical Review Letters* **133,** 116602 (2024).

55. Manda, B. M. & Achilleos, V. Insensitive edge solitons in non-Hermitian topological lattices. *arXiv:2405.05441v1,* 1–6 (2024).

56. Kaplan, A. E. & Meystre, P. Enhancement of the Sagnac effect due to nonlinearly induced nonreciprocity. *Optics Letters* **6,** 590 (1981).

57. Kaplan, A. & Meystre, P. Directionally asymmetrical bistability in a symmetrically pumped nonlinear ring interferometer. *Optics Communications* **40,** 229–232 (1982).

58. Hill, L., Oppo, G.-L., Woodley, M. T. M. & Del'Haye, P. Effects of self- and cross-phase modulation on the spontaneous symmetry breaking of light in ring resonators. *Physical Review A* **101,** 013823 (2020).

59. Xu, G., Nielsen, A. U., Garbin, B., Hill, L., Oppo, G. L., Fatome, J., Murdoch, S. G., Coen, S. & Erkintalo, M. Spontaneous symmetry breaking

of dissipative optical solitons in a two-component Kerr resonator. *Nature Communications* **12** (2021).

60. Woodley, M. T., Hill, L., Del Bino, L., Oppo, G. L. & Del'Haye, P. Self-switching Kerr oscillations of counterpropagating light in microresonators. *Physical Review Letters* **126,** 43901 (2021).

61. Ghosh, A., Hill, L., Oppo, G.-L. & Del'Haye, P. Four-field symmetry breakings in twin-resonator photonic isomers. *Physical Review Research* **5,** L042012 (2023).

62. Del Bino, L., Silver, J. M., Stebbings, S. L. & Del'Haye, P. Symmetry breaking of counter-propagating light in a nonlinear resonator. *Scientific Reports* **7,** 43142 (2017).

63. Alharbi, G. H., Wong, S., Gong, Y. & Oh, S. S. Asymmetrical temporal dynamics of edge modes in Su-Schrieffer-Heeger lattice with Kerr nonlinearity. *Physical Review Research* **6,** L042013 (2024).

64. Su, W. P., Schrieffer, J. R. & Heeger, A. J. Solitons in polyacetylene. *Physical Review Letters* **42,** 1698–1701 (1979).

65. Asbóth, J. K., Oroszlány, L. & Pályi, A. *A Short course on topological insulators: band-structure topology and edge states in one and two dimensions* (Springer, 2016).

66. Zhu, B., Zhong, H., Ke, Y., Qin, X., Sukhorukov, A. A., Kivshar, Y. S. & Lee, C. Topological Floquet edge states in periodically curved waveguides. *Physical Review A* **98,** 013855 (2018).

67. Tan, W., Sun, Y., Chen, H. & Shen, S.-Q. Photonic simulation of topological excitations in metamaterials. *Scientific Reports* **4,** 3842 (2014).

68. Yannopapas, V. Dirac points, topological edge modes, and nonreciprocal transmission in one-dimensional metamaterial-based coupled-cavity arrays. *International Journal of Modern Physics B* **28,** 1441006 (2014).

69. Lan, Z., Chen, M. L., Gao, F., Zhang, S. & Sha, W. E. A brief review of topological photonics in one, two, and three dimensions. *Reviews in Physics* **9,** 100076 (2022).

70. Kerr, J. XL. A new relation between electricity and light: dielectrified media birefringent. *The London, Edinburgh, and Dublin Philosophical Magazine and Journal of Science* **50,** 337–348 (1875).

71. Ho, P. P. & Alfano, R. R. Optical Kerr effect in liquids. *Physical Review A* **20,** 2170–2187 (1979).

72. Boyd, R. W. *Nonlinear Optics* 3rd (Academic Press, Inc, 2008).

73. Maiman, T. H. Stimulated optical radiation in Ruby. *Nature* **187,** 493–494 (1960).

74. Righini, R. Ultrafast optical Kerr effect in liquids and solids. *Science* **262,** 1386–1390 (1993).

75. New, G. *Introduction to nonlinear optics* (Cambridge University Press, 2011).

76. Sutherland, R. L. *Handbook of nonlinear optics* (CRC press, 2003).

77. Marcatili, E. Bends in Optical Dielectric Guides. *Bell System Technical Journal* **48,** 2103–2132 (1969).

78. Bogaerts, W., De Heyn, P., Van Vaerenbergh, T., De Vos, K., Kumar Selvaraja, S., Claes, T., Dumon, P., Bienstman, P., Van Thourhout, D. & Baets, R. Silicon microring resonators. *Laser Photonics Reviews* **6,** 47–73 (2012).

79. Yariv, A., Xu, Y., Lee, R. K. & Scherer, A. Coupled-resonator optical waveguide : a proposal and analysis. **24,** 711–713 (1999).

80. Poon, J., Scheuer, J., Mookherjea, S., Paloczi, G. T., Huang, Y. & Yariv, A. Matrix analysis of microring coupled-resonator optical waveguides. *Optics Express* **12,** 90 (2004).

81. Hill, L., Oppo, G.-L. & Del'Haye, P. Multi-stage spontaneous symmetry breaking of light in Kerr ring resonators. *Communications Physics* **6,** 208 (2023).

82. Haelterman, M., Trillo, S. & Wabnitz, S. Polarization multistability and instability in a nonlinear dispersive ring cavity. *Journal of the Optical Society of America B* **11,** 446 (1994).

83. Woodley, M. T. M., Silver, J. M., Hill, L., Copie, F., Del Bino, L., Zhang, S., Oppo, G.-L. & Del'Haye, P. Universal symmetry-breaking dynamics for the Kerr interaction of counterpropagating light in dielectric ring resonators. *Physical Review A* **98,** 053863 (2018).

84. Strogatz, S. & Dichter, M. *Nonlinear dynamics and chaos* (CRC Press, 2008).

85. Lugiato, L., Prati, F. & Brambilla, M. *Nonlinear optical systems* (Cambridge University Press, 2015).

86. Del Bino, L., Silver, J. M., Woodley, M. T. M., Stebbings, S. L., Zhao, X. & Del'Haye, P. Microresonator isolators and circulators based on the intrinsic nonreciprocity of the Kerr effect. *Optica* **5,** 279 (2018).

87. Shim, J.-B., Schlagheck, P., Hentschel, M. & Wiersig, J. Nonlinear dynamical tunneling of optical whispering gallery modes in the presence of a Kerr nonlinearity. *Physical Review A* **94,** 053849 (2016).

88. Coen, S., Garbin, B., Xu, G., Quinn, L., Goldman, N., Oppo, G.-L., Erkintalo, M., Murdoch, S. G. & Fatome, J. Nonlinear topological symmetry protection in a dissipative system. *Nature Communications* **15,** 1398 (2024).

89. Ghosh, A., Pal, A., Hill, L., Campbell, G. N., Bi, T., Zhang, Y., Alabbadi, A., Zhang, S. & Del'Haye, P. Controlled light distribution with coupled microresonator chains via Kerr symmetry breaking. *Photonics Research* **12,** 2376 (2024).

90. Haus, H. H. *Waves and fields in optoelectronics* (Prentice Hall, 1983).

91. Suh, W., Wang, Z. & Fan, S. Temporal coupled-mode theory and the presence of non-orthogonal modes in lossless multimode cavities. *IEEE J. Quantum Electron.* **40,** 1511–1518 (2004).

92. Bitha, R. D. D., Giraldo, A., Broderick, N. G. R. & Krauskopf, B. Bifurcation analysis of complex switching oscillations in a Kerr microring resonator. *Phys. Rev. E* **108,** 064204 (6 2023).

93. Cao, Q.-T., Liu, R., Wang, H., Lu, Y.-K., Qiu, C.-W., Rotter, S., Gong, Q. & Xiao, Y.-F. Reconfigurable symmetry-broken laser in a symmetric microcavity. *Nature Communications* **11,** 1136 (2020).

94. Longhi, S., Kominis, Y. & Kovanis, V. Presence of temporal dynamical instabilities in topological insulator lasers. *EPL (Europhysics Letters)* **122,** 14004 (2018).

95. Wong, S., Olthaus, J., Bracht, T. K., Reiter, D. E. & Oh, S. S. A machine learning approach to drawing phase diagrams of topological lasing modes. *Communications Physics* **6,** 104 (2023).

96. D'Alessandro, G. & Oppo, G.-L. Gauss-Laguerre modes: a "sensible" basis for laser dynamics. *Optics Communications* **88,** 130–136 (1992).

97. Schmid, P. J. Dynamic mode decomposition of numerical and experimental data. *Journal of Fluid Mechanics* **656,** 5–28 (2010).

98. H. Tu, J., W. Rowley, C., M. Luchtenburg, D., L. Brunton, S. & Nathan Kutz, J. On dynamic mode decomposition: Theory and applications. *Journal of Computational Dynamics* **1,** 391–421 (2014).

99. Kutz, J. N., Brunton, S. L., Brunton, B. W. & Proctor, J. L. *Dynamic mode decomposition: data-driven modeling of complex systems* (SIAM-Society for Industrial and Applied Mathematics, 2016).

100. Srinivasan, S., Prasad, S., Patil, S., Lazarou, G. & Picone, J. *Estimation of Lyapunov spectra from a time series* in *Conference Proceedings - IEEE SOUTHEASTCON* (IEEE, 2006), 192–195.

101. Oppo, G.-L. & Firth, W. J. Theory and application of cavity solitons in photonic devices. *Philosophical Transactions of the Royal Society A: Mathematical, Physical and Engineering Sciences* **382** (2024).

102. Heebner, J., Vincent Wong, Schweinsberg, A., Boyd, R. & Jackson, D. Optical transmission characteristics of fiber ring resonators. *IEEE Journal of Quantum Electronics* **40,** 726–730 (2004).